

Development of a new photon detector for the A4-Compton backscattering polarimeter at MAMI

Diploma thesis by
María Carmen Mora Espí

Institut für Kernphysik
Johannes Gutenberg-Universität Mainz
August 2007

al tío Nofre i a l'agüelo

Contents

1	Introduction	1
2	The A4 Experiment	3
2.1	Strangeness in nucleon	3
2.2	Parity violating asymmetry	3
2.3	A4 Experimental setup	5
2.4	Measurements	8
3	A4-Compton backscattering polarimeter	9
3.1	Compton polarimetry	9
3.2	Setup of the A4-Compton Backscattering Polarimeter	15
3.2.1	Laser and resonator	16
3.2.2	Beam positioning	18
3.2.3	Photon and fibre detectors	20
3.2.4	Photon tagging and energy calibration	21
3.3	Comparison with other polarimetry methods	23
4	Photon detector	27
4.1	Last detector materials	27
4.1.1	BaF ₂	28
4.1.2	PbWO ₄	29
4.2	LYSO detector	31
4.2.1	Mechanical construction	33
4.3	Detector positioning	34

Contents

5	Measurements	35
5.1	First tests with the detectors	35
5.2	Measurements with radioactive sources	40
5.3	ADC tests	55
5.4	Measurements with the beam	57
5.4.1	Different fibres in trigger	58
5.4.2	Correlation Measurements	61
5.4.3	LYSO high voltage calibration	66
5.5	Measurement of backscattered photons	68
6	Conclusions and outlook	71
	List of Figures	75
	List of Tables	77
	Bibliography	79
	Danksagung	81

Chapter 1

Introduction

Since 1996 the A4-Collaboration is investigating the contribution of the strange quarks to the nucleon form factors by scattering polarized electrons off unpolarized nucleons.

In the constituent quark model the nucleons are formed by three light quarks, udd for neutron and duu for proton, in a sea of virtual gluons which can split in quark-antiquark pairs. Although the nucleons have no net strangeness at all, the influence of strange quarks could still be substantial. The influence of c , b and t is negligible due to their high masses.

In quantum chromodynamics the parity violating asymmetry in the scattering of polarized electrons off unpolarized protons can be calculated with the assumption of no strangeness contribution. Any measurable deviation from this value is an evidence of a pure quark sea effect.

Due to the fact that only linear combinations of the form factors can be extracted from the measurements for each kinematics, different kinematics have been studied for a fixed momentum transferred. From each one, another linear combination is calculated and the electric and magnetic form factors can be separated.

The measured asymmetry depends on the polarization of the electron beam and, in order to extract the real asymmetry, this polarization has to be well known. Therefore, a method to determine the polarization accurately is needed.

Currently the beam polarization is measured with a Møller polarimeter from the A1-Collaboration. Also, measurements after the injector linac of the accelerator next to the electron source are done with a Mott polarimeter, and one transmission Compton polarimeter is fully working in one of the A4 experimental halls. Another polarimeter, the Compton backscattering polarimeter, is being developed by the A4-Collaboration and in this diploma thesis the construction and tests performed with a new photon detector which

Chapter 1. Introduction

is part of this polarimeter are described.

In the next chapter the main A4 experiment is described as well as the results we want to achieve. The third chapter shows the basis of the Compton backscattering polarimeter and its main items and construction. The fourth chapter concentrates on the photon detector and the properties of different materials which have been tested are discussed. Finally the fifth and sixth chapters show the tests and measurements carried out with the detectors and conclusions respectively.

Chapter 2

The A4 Experiment

2.1 Strangeness in nucleon

The constituents of matter are protons, neutrons and electrons. The electrons are point-like particles without structure, so that they are considered as elementary particles. But neutrons and protons have an internal structure. In the constituent quark model, they are formed by three quarks. The proton is formed by two u-quarks and one d-quark and the neutron by two d-quarks and one u-quark.

But we can still look in more detail inside the nucleons. The quarks are confined inside the nucleons due to the strong interaction. The force mediators are gluons, and they can split into quark-antiquark pairs as describes quantum chromodynamics.

The light quarks are up (u), down (d) and strange (s), and the heavy are charm (c), bottom (b) and top (t). Because of their mass, the probability for creation of light quarks from gluons splitting is higher, therefore is easier to find in the quark sea contribution of light quarks than those of heavy quarks.

2.2 Parity violating asymmetry

In the Born approximation, the elastic scattering of electrons off nucleons is described by the exchange of single bosons (Figure 2.1). In the electroweak theory the photon mediates the electromagnetic interaction and the Z^0 -boson mediates the neutral current of the weak interaction.

The contribution of the exchange of Z^0 -bosons to the cross section of the elastic $\vec{e} - p$ scattering is strongly suppressed as compared to the electromagnetic contribution due to its high mass ($m_{Z^0} \approx 92 \text{ GeV}/c^2$). The parity violation in the weak interaction can be used to measure the asymmetry in

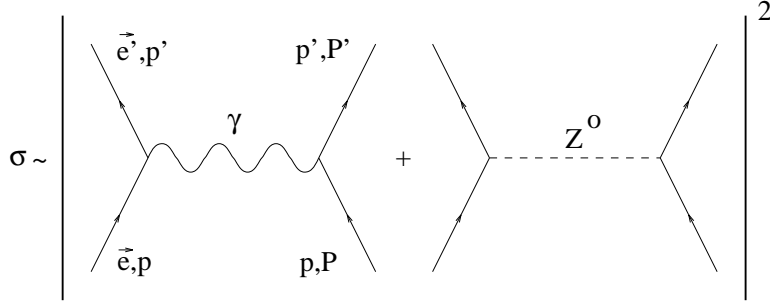


Figure 2.1: Feynman diagram for the scattering of electrons off protons.

the cross sections of the elastic scattering of polarized electrons with different helicities off unpolarized protons.

The parity violating asymmetry is defined as:

$$A = \frac{\sigma^+ - \sigma^-}{\sigma^+ + \sigma^-} \quad (2.1)$$

where σ^+ denotes the cross section in the scattering of right-handed polarized electrons off protons and σ^- of left-handed polarized electrons.

The cross section is calculated from the matrix element of the exchange of one photon and one Z^0 :

$$\sigma \propto |\mathcal{M}_\gamma + \mathcal{M}_Z|^2 \quad (2.2)$$

$$= |\mathcal{M}_\gamma|^2 + 2|\mathcal{M}_\gamma||\mathcal{M}_Z| + |\mathcal{M}_Z|^2 \quad (2.3)$$

Due to the high mass of the Z^0 boson, the term $|\mathcal{M}_Z|^2$ is strongly suppressed as compared to the interference term. The pure photon exchange term does not contribute to the parity violation. The expected value for such an asymmetry is:

$$A \approx \frac{\mathcal{M}_Z}{\mathcal{M}_\gamma} \approx 10^{-6} \quad (2.4)$$

The asymmetry is expressed as a function of the electromagnetic form factors of the nucleon $G_{E,M}^p$, the neutral weak vector form factors of the nucleon $\tilde{G}_{E,M}^p$ and the neutral weak axial form factor of the nucleon \tilde{G}_A^p as [M⁺94]:

$$A = -\frac{G_\mu Q^2}{4\pi\alpha\sqrt{2}} \times \frac{\epsilon G_E^p \tilde{G}_E^p + \tau G_M^p \tilde{G}_M^p - (1 - 4\sin^2\theta_w)\epsilon' G_M^p \tilde{G}_A^p}{\epsilon(G_E^p)^2 + \tau(G_M^p)^2} \quad (2.5)$$

without weak radiative corrections.

This asymmetry can be separated in three terms which depend on the known electromagnetic form factors $G_{E,M}^p$, the unknown strange electromagnetic form factors $G_{E,M}^s$, which are to be measured, and the weak axial form factors \tilde{G}_A^p , using isospin and charge symmetry:

$$A = A_V + A_S + A_A = A_0 + A_S \quad (2.6)$$

where the two terms A_V and A_A represent the asymmetries arising from the vector coupling and the axial coupling respectively at the proton vertex. In the vector term the strangeness contribution has been taken out. These terms, including the weak radiative corrections, are separately [M⁺94]:

$$A_V = -\frac{G_\mu Q^2}{4\pi\alpha\sqrt{2}}\rho'_{eq} \left\{ (1 - 4\hat{\kappa}'_{eq}\hat{s}_Z^2) - \frac{\epsilon G_E^p G_E^n + \tau G_M^p G_M^n}{\epsilon(G_E^p)^2 + \tau(G_M^p)^2} \right\} \quad (2.7)$$

$$A_A = \frac{G_\mu Q^2}{4\pi\alpha\sqrt{2}} \left\{ \frac{(1 - 4\hat{s}_Z^2)\sqrt{1 - \epsilon^2}\sqrt{\tau(1 + \tau)}G_M^p\tilde{G}_A^p}{\epsilon(G_E^p)^2 + \tau(G_M^p)^2} \right\} \quad (2.8)$$

$$A_S = \frac{G_\mu Q^2}{4\pi\alpha\sqrt{2}}\rho'_{eq} \left\{ \frac{\epsilon G_E^p G_E^s + \tau G_M^p G_M^s}{\epsilon(G_E^p)^2 + \tau(G_M^p)^2} \right\} \quad (2.9)$$

with

G_μ	$= 1.16637(1) \cdot 10^{-5} \text{ GeV}^{-2}$	Fermi coupling constant [Par]
α	$= 1/137.03599911(46)$	fine-structure constant [Par]
Q^2		negativ transferred momentum
τ	$= Q^2/4m_p^2$	kinematic parameter
m_p	$= 938.272029(80)\text{MeV}/c^2$	Proton mass [Par]
ϵ	$= [1 + 2(1 + \tau) \tan^2 \frac{\Theta}{2}]^{-1}$	kinematic parameter
ϵ'	$= \sqrt{1 - \epsilon^2}\sqrt{\tau(1 + \tau)}$	kinematic parameter
\hat{s}_Z^2	$= 0.23120(15)$	weak-mixing angle $\sin \theta_w(m_Z)_{\overline{MS}}$ [Par]
Θ	$= 32.1^\circ - 38.5^\circ$	scattering angle in lab frame
ρ'_{eq}	$= 0.9878$	electroweak radiation correction [Par]
$\hat{\kappa}'_{eq}$	$= 1.0027$	electroweak radiation correction [Par]

2.3 A4 Experimental setup

The magnitude of the asymmetry which is measured in the experiment is between 10^{-5} and 10^{-6} , and the absolut accuracy that we want to achieve is of the order of $\approx 10^{-7}$. This requires a large number of events (10^{13} – 10^{14}

Chapter 2. The A4 Experiment

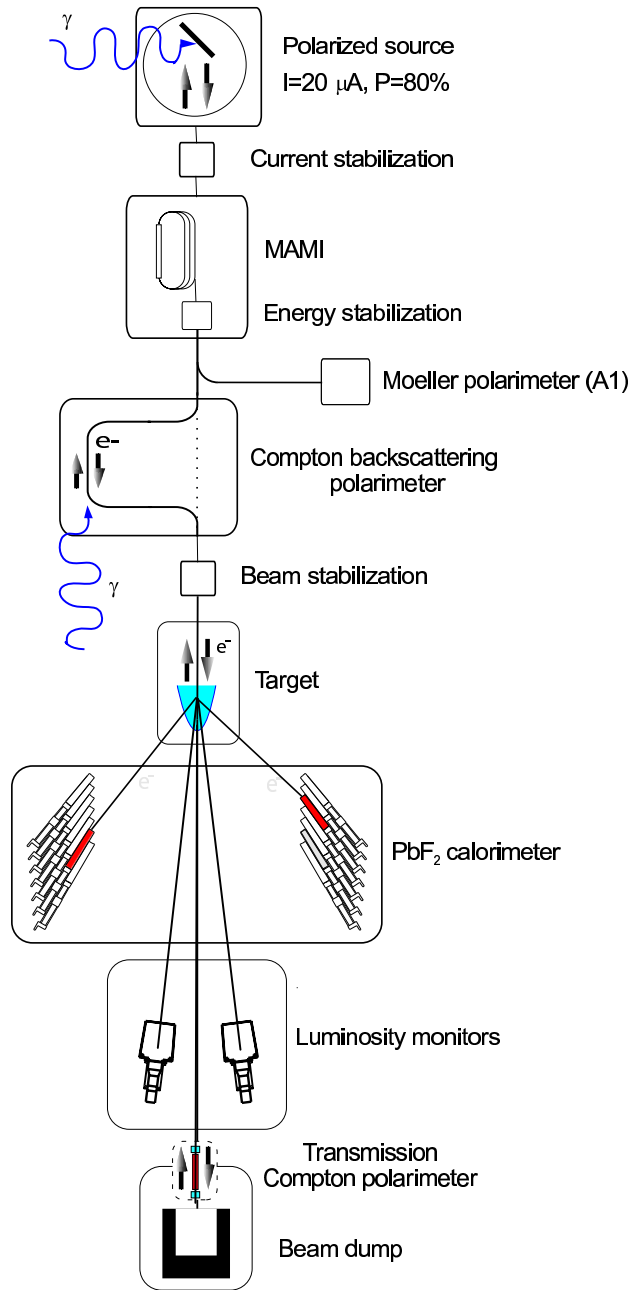


Figure 2.2: Schematic drawing of the experimental setup of the A₄ experiment. In the MAMI facility, polarized electrons are accelerated up to 1.5 GeV and scattered by an unpolarized liquid hydrogen or deuterium target. The scattered electrons are measured in a PbF₂ calorimeter. The luminosity monitors measure the scattered particles under small angles in order to correct the fluctuations in the density of the target. The beam polarization is measured by three polarimeters. The current, energy and position of the beam are measured and stabilized in different points of the beam line

counts) at high luminosity ($(0.5-1.0)10^{34} \text{ s}^{-1} \text{ cm}^{-2}$) and high rates (100 MHz) in the detector. In order to measure these asymmetries, a fast calorimeter of large acceptance is required.

The figure 2.2 shows a schematic drawing of the whole A4-experimental setup.

The polarized source in the MAMI facilities emits polarized electrons with an intensity of $20 \mu\text{A}$ and a polarization degree of about 80%. The maximal energy which can be achieved is now 1.5 GeV, but in our experiment we have used 855 MeV, 570 MeV and 315 MeV so far. Measurements with higher energies will be done in the future.

The electrons are scattered by a target 10 cm long when measurements at forward angles are carried out and 20 cm long when the measurements are at backward angles. In the first measurements the target was a hydrogen target and now deuterium is being used.

The calorimeter used in the A4 experiment is a 1022 channel PbF_2 -Cherenkov calorimeter. It can be arranged under forward ($30^\circ-40^\circ$) or backward ($140^\circ-150^\circ$) angles in order to measure with different kinematics [Glä05]. For each crystal of the calorimeter there is an electronic circuit where the photomultiplier signal of the crystal and its 8 closest neighbours is digitized. The digitized information is then histogrammed. The parity violating asymmetry is extracted from the analysis of these histograms.

Behind the target, eight luminosity monitors detect the scattered particles under small angles ($4.4^\circ-10^\circ$) to correct the data from fluctuations in the target density.

A system of beam monitors has also been developed. With these beam monitors, the beam properties, like position, angle, energy and current, can be measured with high precision. These signals are used in the beam stabilization and the monitored values are used to decorrelate the measured asymmetry from the influence of beam parameter fluctuations.

The electron beam polarization is measured using a Møller polarimeter developed by the A1-Collaboration [Str00]. With this polarimeter, the polarization can be measured once per week, and these measurements need interpolation between them. This polarization measurement is destructive for the electron beam and has to be carried out under completely different beam conditions than those in our experiment.

In order to avoid this destructive measurement, two Compton polarimeters have been developed by the A4-Collaboration. The transmission Compton polarimeter is located in front of the beam dump and uses the polarization transfer from the electron beam to the bremsstrahlung photons

which are produced in the target. The polarization dependent transmission of bremsstrahlung photons through a permanent magnet in front of the beam dump is used for a relative measurement of the polarization of the electron beam [Wei00].

The laser Compton backscattering polarimeter uses the cross section asymmetry in the scattering of circularly polarized photons on longitudinally polarized electrons to measure the beam polarization. It can measure the absolute longitudinal electron beam polarization online, while the main experiment is running.

2.4 Measurements

The A4-Collaboration at MAMI is investigating the influence of strange quarks on the electric and magnetic form factors of the nucleon with electron scattering experiments. From asymmetry measurements, only linear combination of these form factors can be calculated. At different kinematics, one has different linear combinations and the electric and magnetic form factors can be separated using the Rosenbluth separation.

At the very beginning the elastic scattering between polarized electrons of 855 MeV at $\theta = 35^\circ$ on protons was studied. It is related to a transferred momentum $Q^2 = 0.23(\text{GeV}/c)^2$ [M⁺04]. Under these conditions, we obtain a linear combination of the electric and magnetic form factors of $G_E^s + 0.225G_M^s = 0.039 \pm 0.034$ which is proportional to the measured physics asymmetry $A_{phys} = (-5.44 \pm 0.54_{(stat)} \pm 0.26_{(sys)})\text{ppm}$ [M⁺04]. The first error represents the statistical accuracy and the second error represents the systematical uncertainties including beam polarization.

After that, measurements at 570 MeV, which corresponds to a transferred momentum of $Q^2 = 0.11(\text{GeV}/c)^2$ for the same angle, were carried out [M⁺05]. With these measurements, linear combinations of the magnetic and electric form factors can be determined. The measured asymmetry in this case was $A_{phys} = (-1.36 \pm 0.29_{(stat)} \pm 0.13_{(sys)})\text{ppm}$. The extracted contribution to the electromagnetic form factors from the data is now $G_E^s + 0.106G_M^s = 0.071 \pm 0.036$ [M⁺05].

Then to have access to the magnetic form factors independently, the rearrangement of the calorimeter at backward angles ($\theta = 145^\circ$) was performed [Glä05]. To achieve the same transferred momentum as with measurements at 855 MeV and $\theta = 35^\circ$ the needed beam energy is 315 MeV. Currently measurements with 315 MeV on deuterium are carried out.

Chapter 3

A4-Compton backscattering polarimeter

The measured asymmetry in the main experiment depends on the polarization of the electron beam.

$$A_{exp} \sim A_{phys} P_e \quad (3.1)$$

This polarization is measured with different polarimeters, but only if one uses the method of Compton backscattering polarimetry, measurements during the main experiment is running can be done

3.1 Compton polarimetry

Compton polarimetry is based on the Compton effect which occurs when scattering between photons and quasi-free fermions takes place. The cross section of the effect depends on the polarization of the incoming particles.

In the A4 Compton backscattering polarimeter this is implemented by the interaction of laser light with the electron beam.

The kinematics of Compton effect is easier to describe if one uses the electron rest frame. Variables in rest frame will be represented with a prime sign ($'$), others correspond to laboratory frame. The transition to the laboratory frame will be done using the Lorentz-transformation. In the calculation the z -axis will be considered as the direction of the electron momentum (\vec{p}_i). Consider now one photon with initial momentum \vec{k}_i coming to the electron in the xz -plane under an angle θ_i with z -axis (Figure 3.1). The backscattered photon exits with momentum \vec{k}_f under an angle θ_f with respect to the z -axis.

In the electron rest frame, using 4-momentum conservation, the final

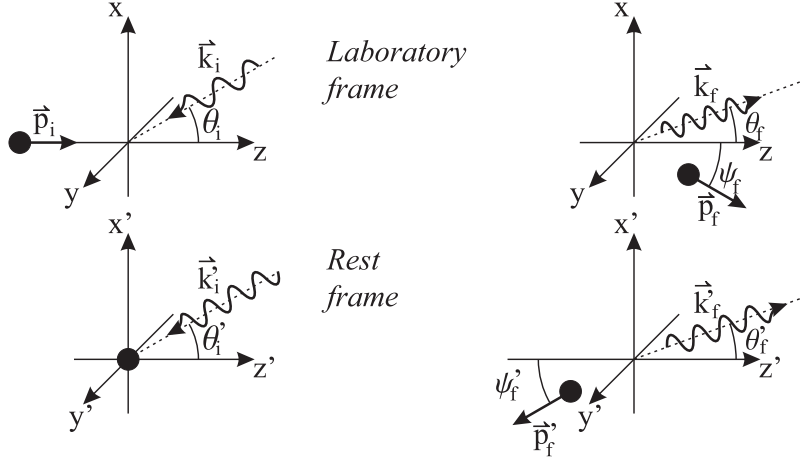


Figure 3.1: Kinematics of the Compton effect with the angle definitions. Right: before scattering; left: after scattering. Variables in rest frame are represented with a prime sign ($'$), others are variables in laboratory frame.

energy of the photon, k'_f , depending on its initial energy, k'_i , and initial and final angles, θ'_i and θ'_f , is [Ima03]:

$$k'_f(\theta'_f, \theta'_i) = \frac{k'_i}{1 + \frac{k'_i}{m_0} [1 + \cos(\theta'_f - \theta'_i)]} \quad (3.2)$$

where m_0 is the electron rest mass. The dependencies on the angles between laboratory and rest frame are calculated using the Lorentz-transformation:

$$\cos \theta'_i = \frac{\beta + \cos \theta_i}{1 + \beta \cos \theta_i} \quad \sin \theta'_i = \frac{\sin \theta_i}{\gamma (1 + \beta \cos \theta_i)} \quad (3.3)$$

$$\cos \theta'_f = \frac{\cos \theta_f - \beta}{1 - \beta \cos \theta_f} \quad \sin \theta'_f = \frac{\sin \theta_f}{\gamma (1 - \beta \cos \theta_f)} \quad (3.4)$$

The relations between initial and final energies in the laboratory and rest frame are:

$$k'_i = \gamma (1 + \beta \cos \theta_i) k_i \quad (3.5)$$

$$k_f = \gamma (1 + \beta \cos \theta'_f) k'_f \quad (3.6)$$

$$\Rightarrow k_f = \gamma^2 f(k_i) \quad (3.7)$$

The magnitudes β and γ are the relativistic parameters of the electron.

3.1 Compton polarimetry

According to the equation 3.5, the photon gains energy from being Lorentz boosted twice. For a highly relativistic electron beam ($\gamma \gg 1$) this makes the detection of the backscattered photons possible.

$$k_f(\theta_f) = (1 + \beta) \frac{k_i}{1 - \beta \cos \theta_f + \frac{k_i}{\gamma m_0} (1 + \cos \theta_f)} \quad (3.8)$$

In our case these energies have to be measured in the photon calorimeter as well as the number of photons which have interacted with the electrons of the beam, since depending on the polarization the cross sections are different.

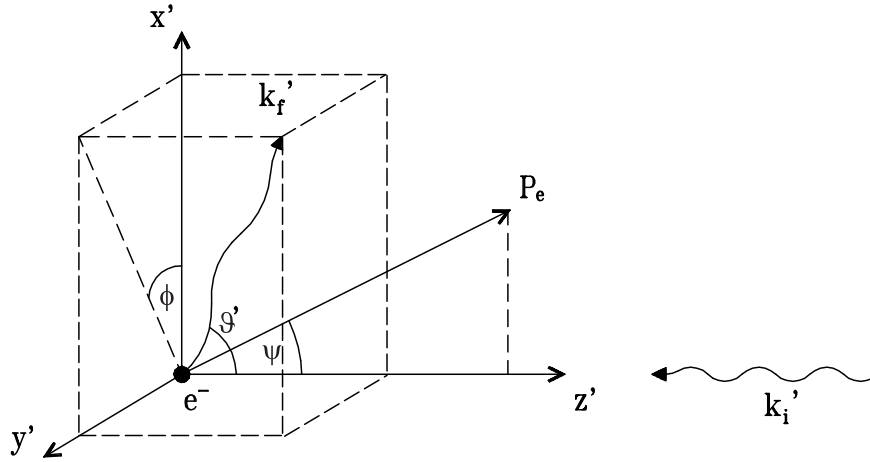


Figure 3.2: Compton scattering and the polarization of the electrons. Variables with a prime sign describe the rest frame, ψ represents the electron polarization angle, ϑ' is the scattering angle and ϕ its projection in the x' - y' plane. This variable, ϕ , has the same value in the rest and the laboratory frames.

It is important to know how the Compton cross section can be described as a function of the polarization states of electrons and photons.

The total Compton cross section can be separated in three terms as follows [LG96]:

$$\frac{d\sigma}{d\Omega} = \frac{d\sigma_0}{d\Omega} \mp \cos \psi P_e P_\gamma \frac{d\sigma_p}{d\Omega} \mp \sin \psi P_e P_\gamma \cos \phi \frac{d\sigma_a}{d\Omega} \quad (3.9)$$

Here, ψ represents the polarization angle of the electrons, $P_e P_\gamma$ is the product of the polarizations of electron and photon beams and ϕ is the azimuthal scattering angle of photons. The plus and minus signs come from the value of the polarization of the electron and laser beams. Right-handed electrons and right polarized light are considered positive polarized and left-handed electrons as well as left polarized light as negative.

Chapter 3. A4-Compton backscattering polarimeter

The cross section has one term, $d\sigma_0/d\Omega$, which does not depend on electron polarization, another one which depends on transversal electron polarization, which goes with $\sin\psi$, and another one which depends on the longitudinal electron polarization, which goes with $\cos\psi$.

These cross sections are in detail:

$$\frac{d\sigma_0}{d\Omega} = \frac{r_0^2}{2} \left(\frac{k'_f}{k'_i} \right)^2 \left(1 + \cos^2 \theta' + \frac{(k'_i - k'_f)^2}{k'_i k'_f} \right) \quad (3.10)$$

$$\frac{d\sigma_p}{d\Omega} = \frac{r_0^2}{2} \left(\frac{k'_f}{k'_i} \right)^2 \left(\frac{k'_f}{k'_i} - \frac{k'_i}{k'_f} \right) \cos \theta' \quad (3.11)$$

$$\frac{d\sigma_a}{d\Omega} = \frac{r_0^2}{2} \left(\frac{k'_f}{k'_i} \right)^2 \left(1 - \frac{k'_f}{k'_i} \right) \sin \theta' \quad (3.12)$$

where r_0 represents the classical electron radius.

In case of small scattering angles ($\theta \ll 1$), and if we consider $\beta \approx 1$, the transformation from rest frame to laboratory frame is:

$$\cos \theta' = \frac{1 - \gamma^2 \theta^2}{1 + \gamma^2 \theta^2} \quad (3.13)$$

and from equation 3.8, the energy of the backscattered photons is:

$$k_f = \frac{4\gamma^2 k_i}{1 + \frac{4\gamma k_i}{m_e} + \gamma^2 \theta^2} \quad (3.14)$$

In the scope of this work, we consider only longitudinally polarized electrons, so we use an azimuthal averaging detector. Therefore the third term in the equation 3.9 vanishes.

We can now define the reduced energy ρ as follows:

$$\rho = \frac{k_f}{k_{f,max}} = \frac{1 + \frac{4\gamma k_i}{m_e}}{1 + \frac{4\gamma k_i}{m_e} + \gamma^2 \theta^2} = \frac{1}{1 + a\gamma^2 \theta^2} \quad (3.15)$$

where the dimensionless parameter a means

$$a = \frac{1}{1 + \frac{4\gamma k_i}{m_e}} \quad (3.16)$$

3.1 Compton polarimetry

After integration over all ϕ angles, we obtain the differential cross section as a function of ρ in the laboratory frame:

$$\frac{d\sigma}{d\rho} = \frac{d\sigma_0}{d\rho} \mp P_e P_\gamma \cos \psi \frac{d\sigma_p}{d\rho} \quad (3.17)$$

with:

$$\frac{d\sigma_0}{d\rho} = 2\pi r_0^2 a \left(1 + \frac{\rho^2 (1-a)^2}{1-\rho(1-a)^2} + \left(\frac{1-\rho(1+a)}{1-\rho(1-a)} \right)^2 \right) \quad (3.18)$$

$$\frac{d\sigma_p}{d\rho} = 2\pi r_0^2 a \left((1-\rho(1+a)) \left(1 - \frac{1}{(1-\rho(1-a))^2} \right) \right) \quad (3.19)$$

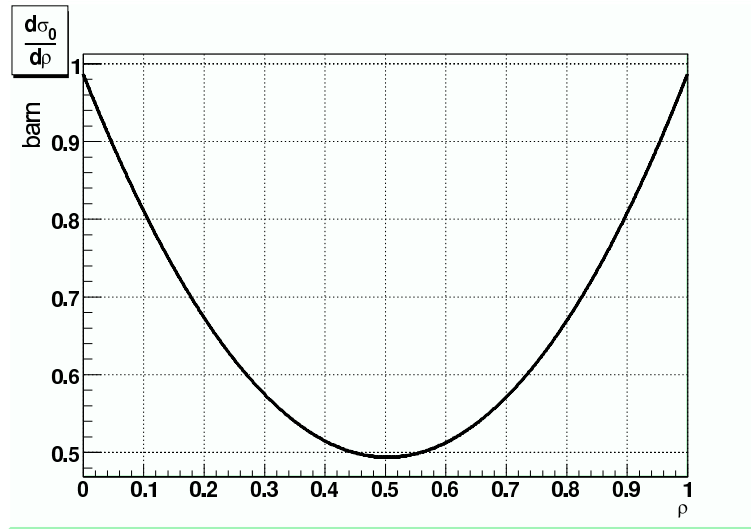


Figure 3.3: *Unpolarized cross section of the Compton effect as a function of the reduced energy, ρ , for a beam energy of 315 MeV and 515.5 nm laser light.*

Figures 3.4 and 3.3 show how the individual cross sections depend on the reduced energy ρ . Since the cross section has one polarization dependent part and another one which is polarization independent, we can calculate the Compton asymmetry as follows:

$$A_{exp} = \frac{N^+ - N^-}{N^+ + N^-} \quad (3.20)$$

where N^+ and N^- are the number of backscattered photons by right-handed and left-handed electrons respectively. It can be related with the theoretical Compton asymmetry for this case as:

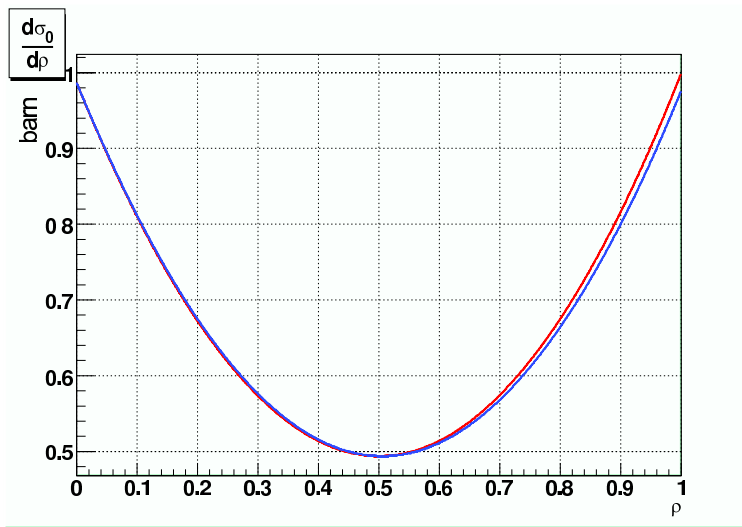


Figure 3.4: Polarized cross section of the Compton effect as a function of the reduced energy, ρ , for a beam energy of 315 MeV and 515.5 nm laser light. Red represents the negative polarization and blue the positive polarization. The difference between both cross sections results in an asymmetry which can be calculated.

$$A_{exp} = P_e P_\gamma A \quad (3.21)$$

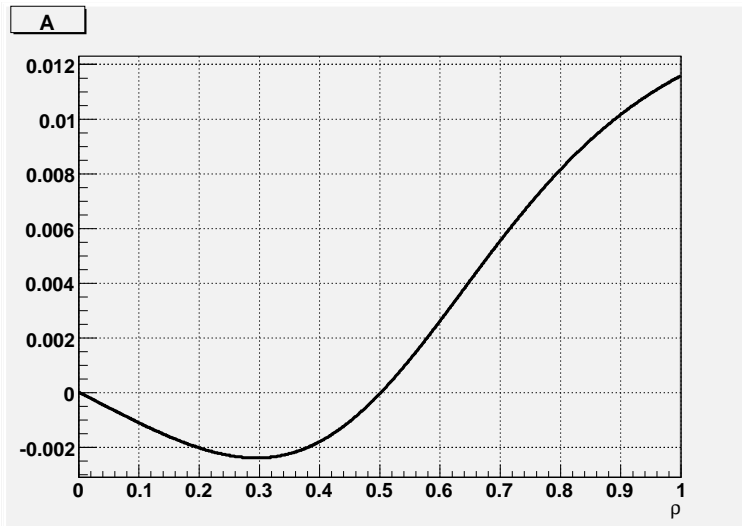


Figure 3.5: Compton asymmetry as a function of the reduced energy ρ , for a beam energy of 315 MeV and 515.5 nm laser light.

The figure 3.5 represents the Compton asymmetry as a function of the reduced energy, ρ .

3.2 Setup of the A4-Compton Backscattering Polarimeter

Note that this is not the same asymmetry which is measured in the main experiment, although due to the parity violation of the electroweak interaction the principles are the same.

There are three methods in order to measure the beam polarization. One differential method is used when the energy of each individual photon can be measured. The integral one measures the total amount of backscattered photons for each laser helicity. The energy weighted method is used if only the total amount of backscattered photons is known for both laser helicities.

In our case, by measuring the differences between rates of backscattered photons by right or left polarized electrons, the absolute polarization of the electron beam can be measured. Also the laser light polarization is switched in order to avoid systematic errors.

3.2 Setup of the A4-Compton Backscattering Polarimeter

In figure 3.6 we can see a schematic drawing of the A4-Compton backscattering polarimeter. It consists of a horizontal chicane formed by four dipole magnets and two quadrupoles. With this system we can bend the electron beam out of its trajectory to be able to overlap it with the laser beam which goes through this displaced region.

Inside the interaction region there are three wire scanners used to measure

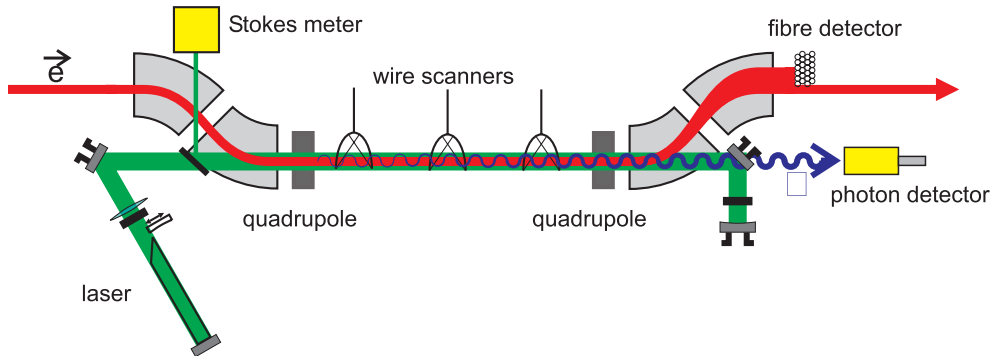


Figure 3.6: Schematic drawing of Compton backscattering polarimeter. The electron beam is bent by four dipole magnets through the interaction region. Two quadrupoles correct the angular dispersion of the beam. Three wire scanners measure the electron and laser beam position in order to overlap them. The backscattered photons are detected in a photon calorimeter placed behind the interaction region. At the end of the chicane, an electron fibre detector is placed to tag the photons.

the position of the laser and electron beams, which is necessary in order to establish overlap between both beams.

Just behind the interaction region, the photon calorimeter, which is the main topic within this diploma thesis, is placed. It detects the photons which have interacted with electrons. The number of backscattered photons depends on the electron spin polarization and the polarization of the laser beam.

Due to residual gas inside the interaction region, the electrons also lose energy by bremsstrahlung. In order to reduce the rates in the photon detector a plastic fibre electron detector is placed at the end of the chicane. The electrons which have suffered interactions are deviated from their original trajectory and consequently from the beam line. They are detected in the fibre detector, which is position sensitive. A coincidence setup to measure with tagged photons is used.

The fibre detector can also be used to perform an energy calibration of the calorimeter. If the position of the fibre which has been hit is known, the corresponding energy for the correlated photon can be calculated. This method is explained in the chapter 5 (section 5.4.2).

The main parts of the polarimeter are described in the next sections.

3.2.1 Laser and resonator

The development of the resonator and the intracavity concept was studied in a diploma thesis [Ima03]. The used laser is an Argon-Ion laser Innova 425 from Coherent. The active medium is an argon plasma with maximal emission at 514.5 nm. This laser can achieve an output power of 25 W in multi-line mode. The measured transmission of the output coupler is around 8%, so inside the resonator the light power is up to 300 W. In order to achieve as high a luminosity as possible, the output coupler has been exchanged by a new mirror with high reflectivity. The resonator has been modified, so that the electron beam is now guided through the resonator to make use of the high intra-cavity intensity. To increase the luminosity further also both laser beam and electron beam are collinear.

The structure of the resonator is shown in figure 3.7. It consists of five elements. The flat mirror, M_1 , and the spherical mirror, M_2 , have both high reflectivity and they are the new end-mirrors of the resonator. The lens L is used to focus the laser beam inside the interaction region.

The other two elements are the wave-plates WP_1 and WP_2 , which are used to polarize the light circularly.

3.2 Setup of the A4-Compton Backscattering Polarimeter

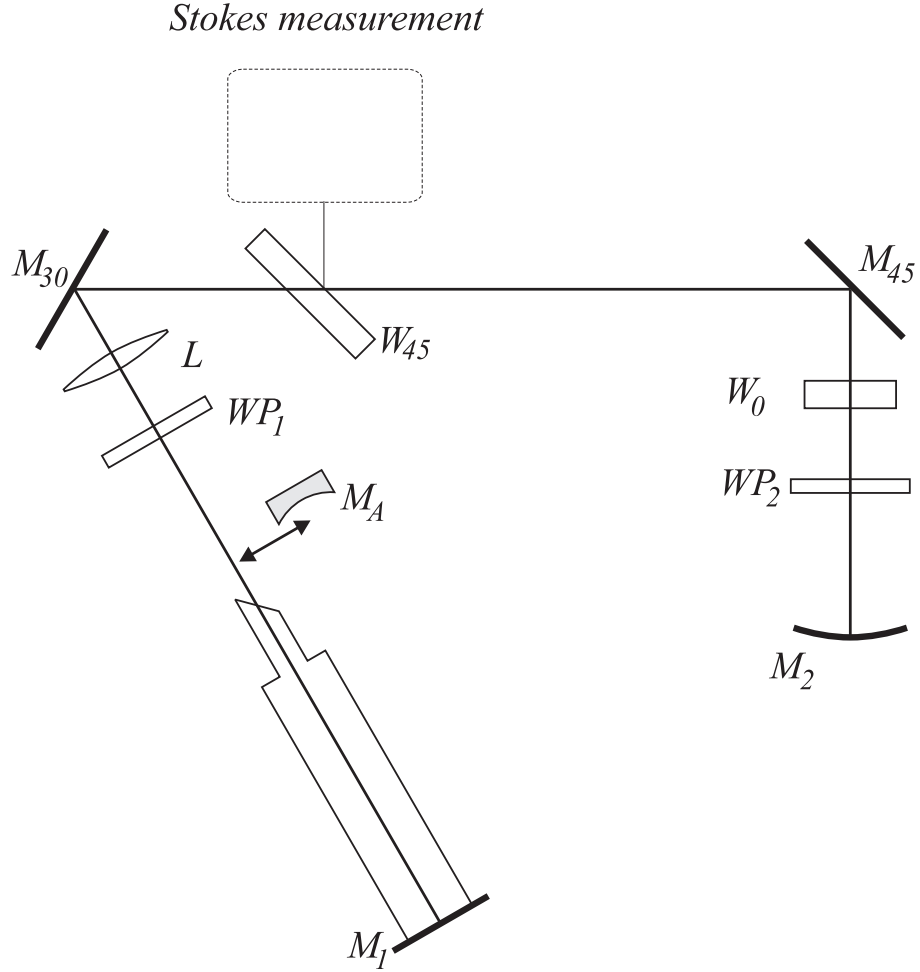


Figure 3.7: Schematic drawing of Laser and resonator. M_1 and M_2 are the end mirrors of the resonator. M_{30} and M_{45} bend the laser beam into the interaction region. W_{45} and W_0 are the vacuum windows, and W_{45} acts as a beam splitter for the Stokes measurement. WP_1 and WP_2 are used to polarize the laser light circularly. L is used to focus the light and M_A is used for the initial optics alignment.

Since the space of which we dispose in the hall is not very long, the resonator has folded geometry, and to achieve this, two more mirrors are used, M_{30} and M_{45} . These mirrors bend the optical axis by angles of 60° and 90° respectively. The M_{30} mirror separates the resonator in one medium arm and one interaction arm. There is also another concave mirror, M_A , issued for the initial optics alignment.

The main part of the optical system is mounted on a precision guide rail from **MiniTec**, placed on a granite plate 10 cm thick, and on a block of expanded polystyrene in order to absorb all the vibrations that can affect

the whole laser system. The rail is fixed on 12 height adjustable aluminum bars which allow the alignment of the rail in horizontal and vertical direction.

The laser beam goes into the interaction zone through the vacuum windows W_0 and W_{45} . One of them is perpendicularly mounted to the beam, but the second one forms an angle of 45° with it. This window works like a beam splitter. This is used to measure the laser beam polarization, i.e. the Stokes parameters of the light.

3.2.2 Beam positioning

To improve the overlap between laser and electron beams we need to determine their axes. For this purpose there are three wire scanners inside the chicane like those which are used in the MAMI beam line .

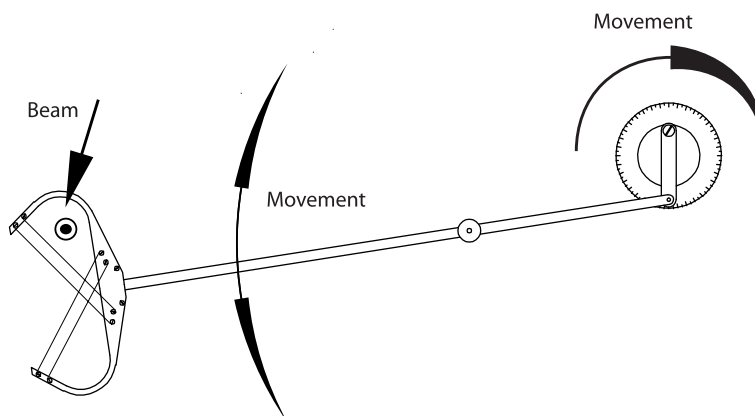


Figure 3.8: *Schematic drawing of the wire scanners. The movement of the disc permits the movement of the wire scanner arm. With this movement, the wires cross the electron and laser beams and it permits to measure their positions.*

The main item is a fork with two pairs of wires which cross in the center of the structure. The fork is mounted on a mobile arm which can move the wires inside the beam pipe through the beam line (figure 3.8).

When one of such wires crosses the electron beam, secondary radiation is generated. This radiation is detected in one Lead-glass Cherenkov counter installed in the Hall3. This signal is recorded as a function of time and it is used to calculate the position of the beam.

For the laser position measurement, the laser light is measured with pho-

3.2 Setup of the A4-Compton Backscattering Polarimeter

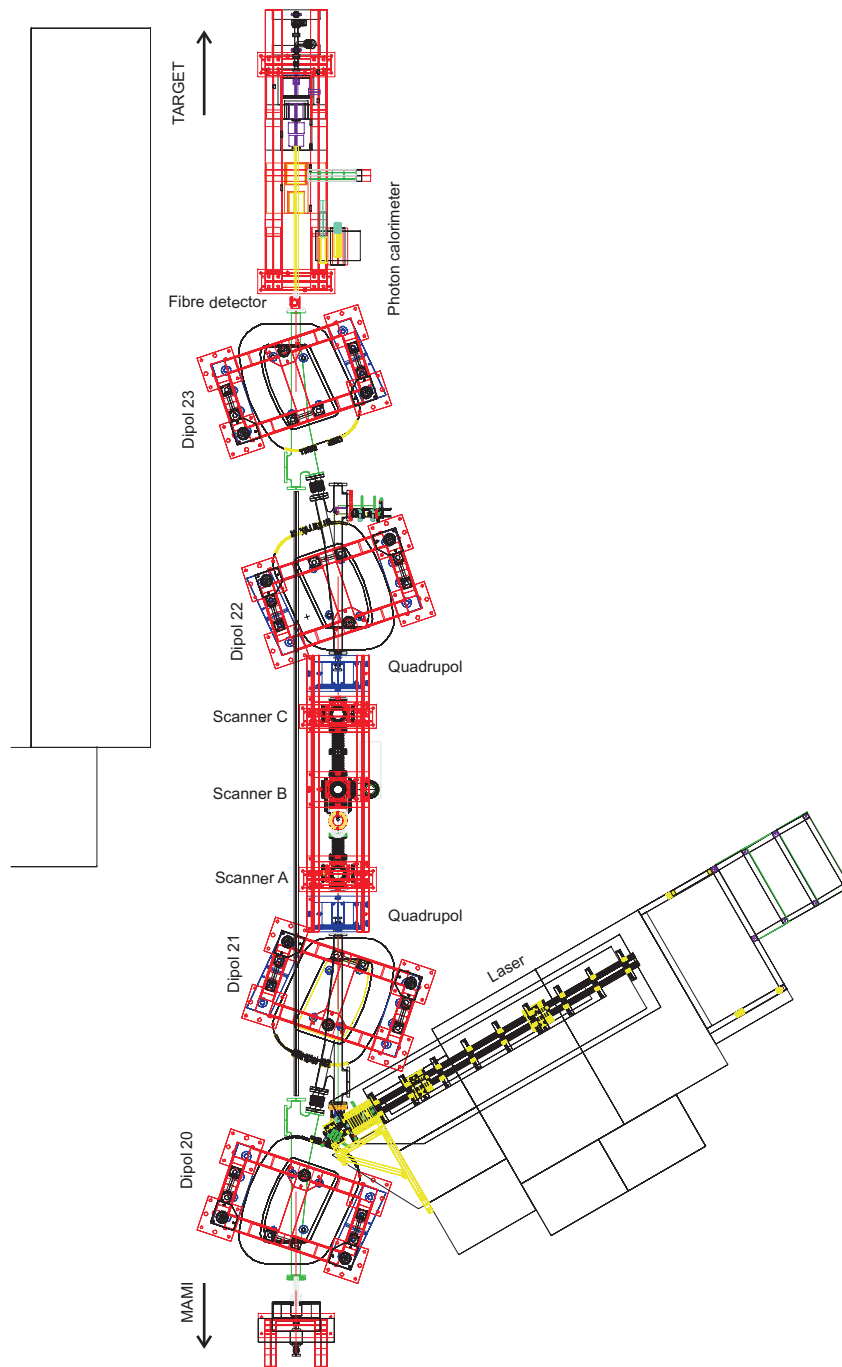


Figure 3.9: AutoCad drawing of A4-Compton Backscattering Polarimeter. The beam from MAMI is bent by four dipole magnets into the interaction region where the electrons are scattered off the photons of the laser. Three wire scanners measure the laser and electron beam positions. At the end of the chicane is placed an electron fibre detector in order to measure with tagged photons in the photon calorimeter, which is placed behind the interaction region.

todiodes. When the wire scanners cut the laser beam, the intensity of light measured in such photodiodes decreases.

The position measurements of both beams do not interfere, so they can be performed simultaneously.

The method used to measure the position of both beams has been developed for a PhD thesis [Lee]. Each scanner is used separately to determine three coordinate pairs (x, y) for each beam. With these coordinates one can determine the beam axes.

The position of both beams can be improved by changing slightly the current flowing through the dipole magnets in the case of the electron beam or by moving the optical elements of the laser setup.

3.2.3 Photon and fibre detectors

The backscattered photons are detected in a calorimeter located behind the interaction region of the chicane. The main part of this diploma thesis is the construction and study of such a detector. Several materials have been tested. These materials and detectors will be described in the next chapter.

In order to calibrate the photon detector and to reduce the readout rates an additional plastic scintillator fibre detector is used. One can see a picture of it in the figure 3.10

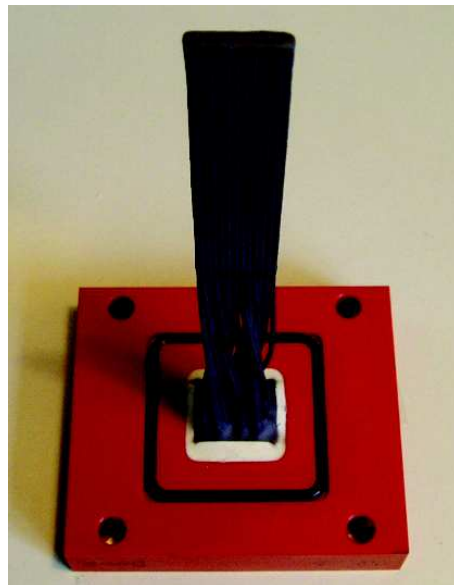


Figure 3.10: *Picture of the actual fibre detector.*

The current version of the fibre detector is formed by 4 layers of 12 fibres

3.2 Setup of the A4-Compton Backscattering Polarimeter

each. The photomultiplier which is used is an **HAMAMATSU H7546**. This is a multianode photomultiplier with 64 pixels.

The light collected in two fibres in the same position of two of the layers of the electron detector go directly to one photomultiplier pixel. As one can see in the figure 3.11, the fibres iA and iB go to the same photomultiplier pixel. Since the fibre detector has 48 fibres, only 24 photomultiplier pixels are used. In the electronics, the signals are summed again in pairs. Two adjacent pairs of fibres form one trigger channel.

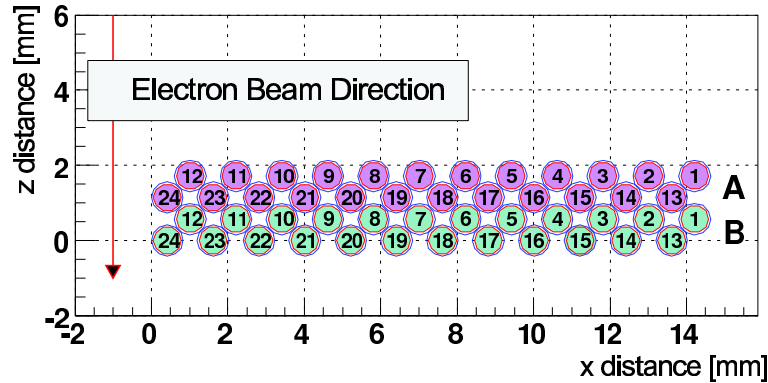


Figure 3.11: Schematic drawing of the fibres layout [Lee]. Fibres with the same number go to one photomultiplier pixel. Two adjacent pairs of fibres form one trigger channel.

Both the fibre and photon detectors can be moved to put them in the best position in relation with the beam line.

3.2.4 Photon tagging and energy calibration

Inside the chicane the electrons lose energy by bremsstrahlung or by Compton effect. In the first case they emit a photon with the same energy as they have lost. If they interact with the laser photons the emitted photons have an energy distribution which is described by the formula 3.8.

These electrons are deviated from their original trajectory due to the dispersion in the dipoles. This deviation depends on the energy loss. To select photons coming from such interactions and reduce the readout rate of the photon detector we have the fibre detector. For our photon detector, bremsstrahlung and Compton scattering are indistinguishable.

The dimensions and position of each fibre in the fibre detector is well known and consequently, also the energy loss of the electrons which hit them.

To have the fibre detector in coincidence with the photon detector reduces the uncorrelated background in the spectra. On the other hand, due to its

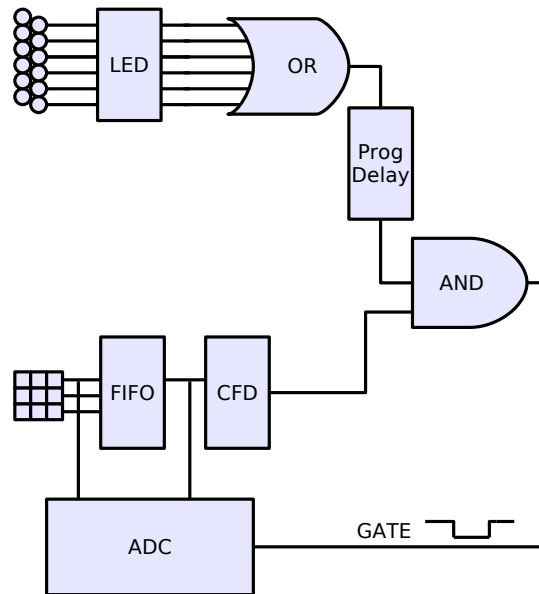


Figure 3.12: Simple schema of the coincidence between fiber and photon detectors.

position sensitivity, the fibre detector can be also used to perform the energy calibration of the calorimeter.

In figure 3.12 one can see the schematics of the electronic system for the coincidence between both detectors.

The fibres of the electron detector can be individually enabled. If one of the fibres which are enabled is hit, the signal has to be accepted by the LED¹. The threshold level is programmed separately for each fibre. Then, after a logic OR the signal is sent to a coincidence unit (AND). If one or more photons have been detected in some of the crystals of the calorimeter, the signal of them is summed in a FIFO², and it has to be accepted by a CFD³. Both signals coming from the fibre and photon detectors have to arrive in coincidence to an AND unit which generates a gate to be sent to the ADC⁴. The relative delay between them can be changed by software. The signal of the individual crystals of the photon detector as well as the sum of all is digitized and histogrammed. Enabling only one fibre we can tag photons with known energy using this setup.

When we have all the trigger channels in coincidence with the calorimeter,

¹Leading Edge Discriminator.

²Fan In - Fan Out unit

³Constant Fraction Discriminator

⁴Analog to Digital Converter.

the spectrum which is measured has to be a continuum of photon counts from the threshold until the maximum energy of the backscattered photons in the acceptance range of the fibre detector.

If only one trigger channel is in coincidence, the measured spectrum shows only a peak corresponding to the photons with the amount of energy which have been lost by the electrons which hit the enabled fibres. These peaks are used to perform an energy calibration of the photon detector.

3.3 Comparison with other polarimetry methods

To measure the polarization of high energy electron beams other types of polarimeters can be used.

In a Møller polarimeter, the polarized electrons of the beam are scattered by a foil of iron and cobalt alloy. With this method the beam is significantly widened up by scattering in the metal foil and therefore the beam can not be used anymore for the main experimental purposes. Furthermore, only measurements with very low currents can be done. With the Møller polarimeter of the A1-Collaboration, one can achieve a statistical accuracy of 2% [Str00].

Another type of polarimeter which can be used is a transmission Compton polarimeter. Such a polarimeter is installed in the A4 facilities at the end of the beam line [Wei00]. Although the polarization measurement with this polarimeter is beam destructing, since it is installed after the target, it does not affect the experiment. The transmission Compton polarimeter is sensitive to the bremsstrahlung photons created in the target and in the scatterers after the collision. The polarization of the secondary radiation depends on the polarization of the original beam. The polarization dependent transmission of bremsstrahlung photons though a permanent magnet permits a relative measurement of the polarization. Then, only fluctuations of the asymmetry can be measured with this polarimeter and the absolute value measured with the Møller polarimeter is used to interpolate with the transmission Compton polarimeter values. This polarimeter can achieve high accuracy in short time in order to measure this variations in the beam polarization.

With a Mott polarimeter, only polarization measurements at very low energies can be done. One of this kind of polarimeter is installed in MAMI facilities next to the injector LINAC.

The Compton backscattering polarimeter is for our purpose the best of all methods because the polarization measurement can be done without destroying the electron beam while the main experiment is running.

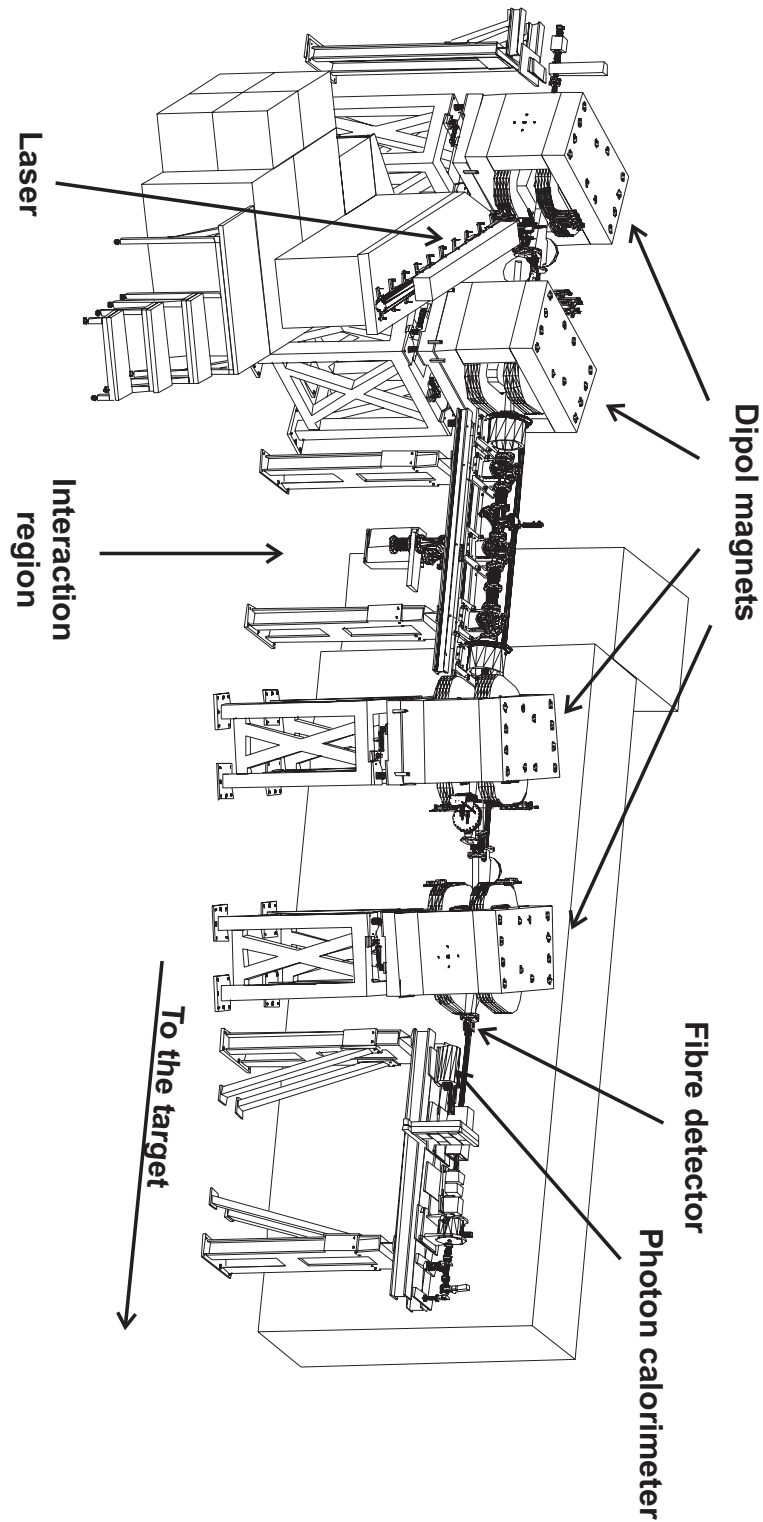


Figure 3.13: 3D view of A4-Compton backscattering polarimeter. One can see where the different parts of the polarimeter are placed.

3.3 Comparison with other polarimetry methods

For a beam energy of 315 MeV the maximum Compton asymmetry is of the order of $A_c^{max} = 1\%$ as we can see in the figure 3.5. We need to detect 10^8 backscattered photons in the photon calorimeter to measure this asymmetry with a relative accuracy of $\Delta A_c^{max} = 1\%$. This number of events can be measured under the actual conditions within 4 days of data taking:

In the last beam time August 2007 we got typically a number of $N = 6 \cdot 10^5$ backscattered photons per 5 minutes with a laser power of 30 W. The signal to noise ratio was 1 : 3. According to [LG96] the measurement time for a given signal to noise ratio R is by a factor of

$$k = 1 + \frac{2}{R} \quad (3.22)$$

longer than without background.

Therefore we need to measure

$$t_{1\%} = \frac{1}{(\Delta A_c^{max})^2} \cdot \frac{5min}{N} \cdot k = 97h \quad (3.23)$$

to achieve 1% relative accuracy.

This is a rough estimation since the Compton asymmetry depends on the energy of the backscattered photons, so the mean asymmetry of the photons that we detect is less than the maximal asymmetry which is used in the calculation.

All four kinds of polarimetry are used in the A4 experiment to obtain interpolated values of the polarization each five minutes with high precision.

Chapter 4

Photon detector

4.1 Last detector materials

Since some years ago different materials have been used for the calorimeter of the Compton backscattering polarimeter. The first detector which was used was a NaI(Tl) detector. It consisted of three cylindric crystals 10.16 cm wide and with a diameter of 20.32 cm [Sik04]. The dimensions of this detector were quite large, and its alignment with the beam interaction region was difficult. It was also done with old materials which did not work properly. There were a lot of problems in the construction and the measurements with this detector and finally it was discarded.

Another material which has been used is BaF₂. This detector was borrowed from TAPS collaboration [Sch89] and its dimensions were smaller. In spite of that, the crystal was supposed to have better energy resolution. The results with this material were approximately the same as with the NaI at the beginning. During the commissioning the origin of background and radiation problems were detected and solved. Nevertheless, we could not achieve the same energy resolution as the TAPS collaboration.

One crystal with higher density, and therefore smaller dimensions, could be easier to shield and it could have better detection efficiency. Since the rates which we have to detect can be high, we also need a faster detector. So a detector of PbWO₄ was tested. Due to the low light yield of this material at room temperature, the detector had to be cooled down to $-25\text{ }^\circ\text{C}$, making use of the dependency of the light yield with the temperature of $d(LY)/dT = -1.9/ - 2.2\text{ } \%/^\circ\text{C}$ at room temperature [Par] [Thi05]. Some results and the experimental setup will be shown in following chapters.

The final detector, which is discussed in this diploma thesis, is built of nine crystals of LYSO¹ ($20 \times 20 \times 200$)mm³ each, arranged to a 3×3

¹LYSO (Lu_{1.8}Y_{.2}Si₅O : Ce) is a cerium doped lutetium based scintillation crystal that

Material	NaI(Tl)	BaF ₂	PbWO ₄ PWO	PbWO ₄ PWO II	LYSO
ρ (g/cm ³)	3.67	4.89	8.3	8.3	7.1
X_0 (cm)	2.59	2.03	0.89	0.89	1.2
$r_{Molière}$ (cm)	4.13	3.10	2.0	2.0	2.37
τ_{decay} (ns)	230	630 ^s 0.9 ^f	50 ^s 10 ^f	5-15	41
λ (nm)	410	300 ^s 220 ^f	560 ^s 420 ^f	420	420
<i>Rel. Output</i> *	100	21 ^s 2.7 ^f	0.1 ^s 0.6 ^f	1	75
<i>Hygroscopic</i>	Yes	No	No	No	No
$d(LY)/dT$ (%/°C)	~ 0	-2 ^s $\sim 0^f$	-1.9	-2.2	~ 0

*Light yield relative to NaI(Tl)

^sSlow component

^fFast component

Table 4.1: *Principal characteristics of the different scintillator materials [Par].*

matrix.

The table 4.1 shows a comparison of the principal characteristics of these materials.

In the next sections the materials which have been tested during the last year are described.

4.1.1 BaF₂

A BaF₂ detector from TAPS collaboration was borrowed to perform some tests with this material. The crystal is 25 cm long and has an hexagonal base with a width across flats of 5.9 cm. At the end of crystal there is a cylindrical section of 2.5 cm of length and a diameter of 5.4 cm which acts as a light guide. On this cylindrical end the photomultiplier is attached. The photomultiplier is a **HAMAMATSU R2059** with diameter 53 mm and 12 dynodes. The faces of the crystal are polished and it is enveloped with teflon and aluminum foil to have a good light collection. To isolate it from external light it is packed with light-proof adhesive tape [Sch89].

offers high density and a short decay time.

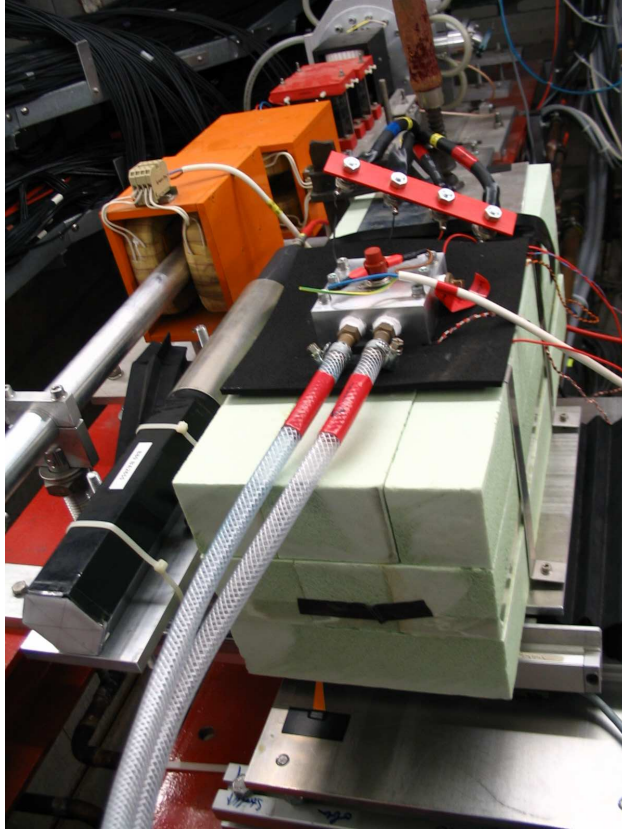


Figure 4.1: *Experimental setup of PbWO₄ and BaF₂ detectors, one next to the other.*

Its radiation length is $X_0 = 2.03$ cm and it has a Molière radius of $r_{Molière} = 3.10$ cm. This material has two scintillating light components, a fast and a slow one. The fast component has a decay time of $\tau_{decay} = 0.9$ ns, since the slow one $\tau_{decay} = 630$ ns. The two components have also different wavelength emission maxima, $\lambda_{max} = 220$ nm and $\lambda_{max} = 300$ nm, respectively. We are interested in a fast detector, but correlation measurements between both components can be done to separate different kinds of particles. The light yield output is also different for each component, 2.7 % in relation with the NaI light yield for the fast component and 21 % for the slow one.

4.1.2 PbWO₄

The PbWO₄ is a more compact material, it was faster than the other ones but very low light yield. It was considered as an alternative if the low energy resolution of our detectors experienced so far would be due to pile-up of background events.

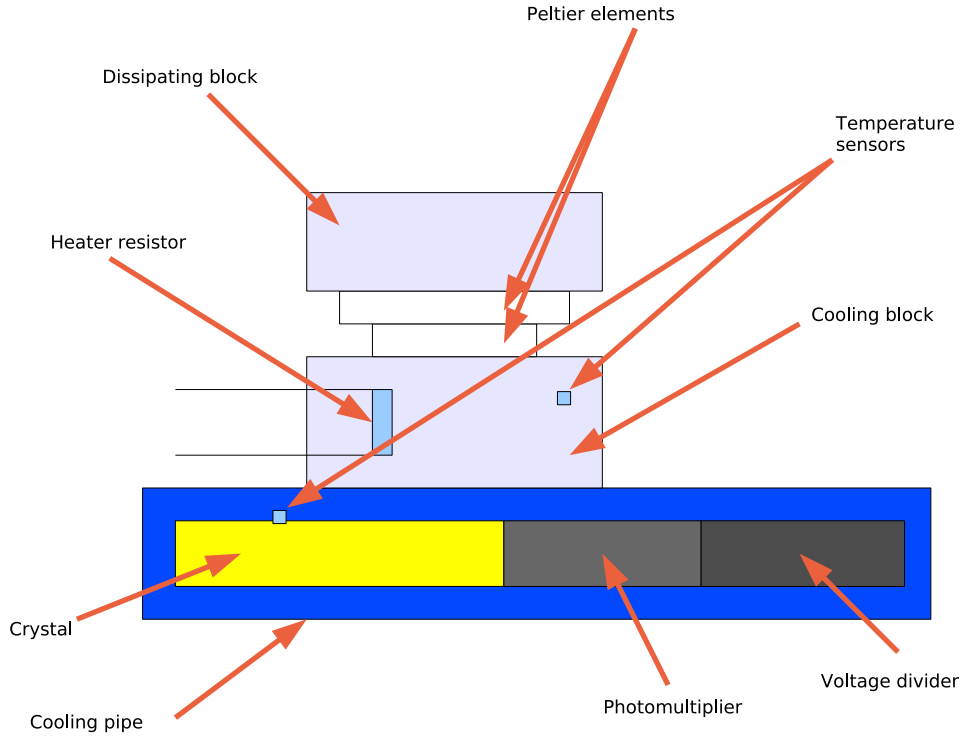


Figure 4.2: *Schematic drawing of the cooling system for PbWO₄.*

An old crystal used by A4-Collaboration some time ago (PWO) and a new one from PANDA collaboration (PWO II) were tested. The photomultipliers that we had to use were quite old, so they had to be tested before. The variation of the light yield with the temperature of this material is strong, $d(LY)/dT = -1.9 \text{ \%}/^\circ\text{C}$ at room temperature for the old crystal and $d(LY)/dT = -2.2 \text{ \%}/^\circ\text{C}$ for the new one. On the other hand, the light yield at room temperature is small, so we had to cool the crystal in order to get sufficiently large signals and energy resolution.

The dimensions of the crystals which were used in the tests were quite similar. The old one, is $(20 \times 20 \times 160) \text{ mm}^3$. The new one, coming from PANDA collaboration, is $(20 \times 20 \times 200) \text{ mm}^3$. The old crystal had yellow color and less transparency than the new one. That is not a damage radiation or ageing in the crystal but the original color of the PWO. PWO II has been improved and it does not have this yellow color. The old crystal was only used to perform the first cooling test with the aim of not breaking the new crystal. Principal characteristics of the new material are a radiation length of $X_0 = 0.89 \text{ cm}$ and a Molière radius of $r_{\text{Molière}} = 2.0 \text{ cm}$. Its peak emission wavelength is $\lambda_{\text{max}} = 420 \text{ nm}$ with a decay time of $\tau_{\text{decay}} = 5 - 15 \text{ ns}$.

The photomultipliers which were used for these crystals were **HAMA-MATSU R6427HA** photomultipliers.

Cooling system

The method which was developed to cool the crystal used two cascaded Peltier elements, a cooling block made of aluminum and a water chiller system. A schematic drawing of the experimental setup is represented in figure 4.2. The main item of this system is the cooling pipe where the crystal together with the photomultiplier and the voltage divider were located. This pipe was an aluminum pipe 37 cm long with square cross section of (6×6) cm². On this pipe there is an aluminum block that extracts heat from the pipe due to the action of the Peltier cascade mounted on top of it. In order to dissipate this heat, another aluminum block is attached to the Peltier elements. This second aluminum block has a hole in which a current of water can flow through. This water current was pumped by a chilling unit which would also cool it. To stabilize the crystal temperature to approximately ± 0.1 °C there are also two heater resistors. Several temperature sensors in different positions of the experimental setup are used to control and survey the temperatures and the heating and cooling powers. To use as less energy as possible and keep a stable temperature, the whole setup was in an isolating box of Polystyrene². A photograph of the complete setup is represented in figure 4.1 together with the BaF₂ detector. With this system, the crystal was cooled down to -25 °C with a stability better than ± 0.1 °C.

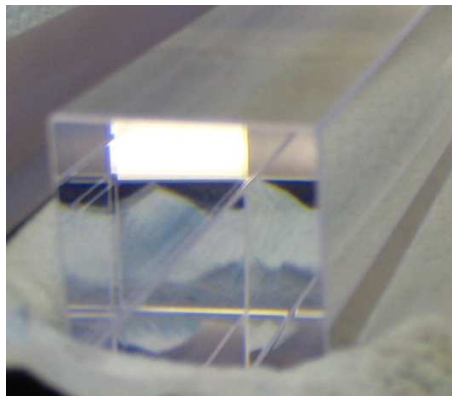


Figure 4.3: *Detail of a LYSO crystal.*

4.2 LYSO detector

For the construction of a new photon detector, nine LYSO crystals from **Saint-Gobain** were ordered (see figure 4.3). The dimensions of these crystals

²Styrodur®

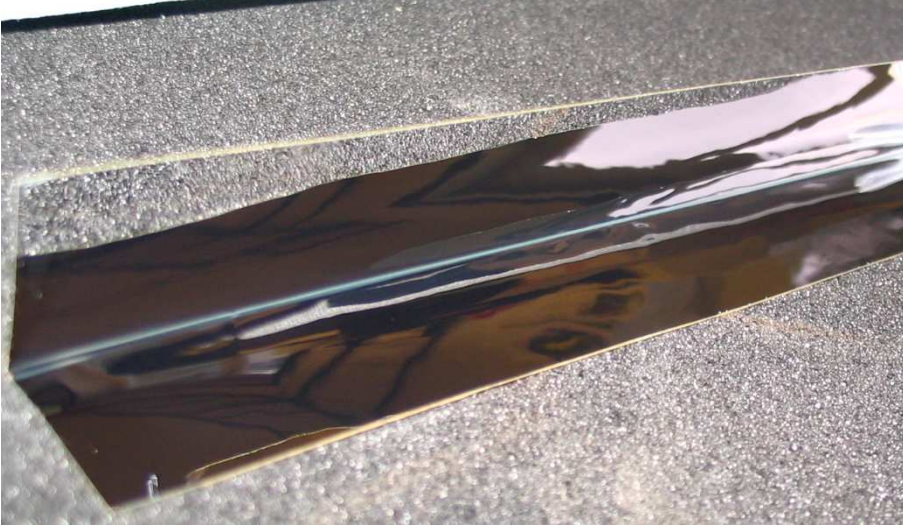


Figure 4.4: Detail of the reflective foil in which the detector is wrapped.

Beam Energy (MeV)	Dispersion (MeV/mm)	Maximal backscattered photon energy (MeV)
315.2	0.88	3.63
570.0	1.60	11.75
854.3	2.40	26.12

Table 4.2: Energy ranges of detected photons as a function of the beam energy.

are $(20 \times 20 \times 200)$ mm³. LYSO is a very compact material with very high light yield, 75 % relative to NaI(Tl). It has a Molière radius of $r_{Molière} = 2.37$ cm and a radiation length of $X_0 = 1.2$ cm. It is also a very fast material, its decay time is $\tau_{decay} = 41$ ns. The peak emission wavelength is also $\lambda_{max} = 420$ nm.

The energy ranges in which the photons have to be detected depend on the beam energy (see table 4.2). Due to the high light yield of LYSO, the required amplification is less than for the other materials, and depending on the beam energy, it has to be more or less.

In our cases, the needed gain was calculated taking into account the light yield of this material and the maximum charge which can be digitized by the ADC. We need a gain of 10^4 for a beam energy of 855 MeV, and a gain of 10^5 when the beam energy is 315 MeV. In order to have in each case the needed amplification, two kinds of photomultipliers from **Photonis** have been used, **XP1912** and **XP1981**, each one to be able to detect photons up to different energies. The base to be used with such photomultipliers is the **Photonis**



Figure 4.5: Detail of one crystal wrapped in reflective foil.

VD108. It is a passive voltage divider, but also active voltage dividers have been built and tested.

A disadvantage of this material is that it has an intrinsic radioactivity. This radioactivity is also measured in the crystal itself. The origin of this radiation is the naturally occurring beta emitter ^{176}Lu , which is part of the compounds of LYSO. ^{176}Lu decays to ^{176}Hf with a branching ratio of 99.66%

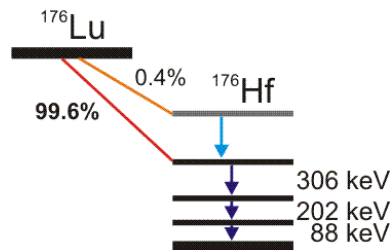


Figure 4.6: LYSO intrinsic radioactivity decay scheme.

to the 597 keV excited state. This state decays with a 3 gamma ray cascade of 307 keV, 202 keV and 88 keV (see figure 4.6). The total rate of this activity is 39 Bq/g. This radioactivity can be treated as part of the background.

4.2.1 Mechanical construction

As already mentioned previously, the LYSO detector consists of a cluster of 9 crystals forming a 3×3 matrix. To collect as much light as possible, each crystal has been wrapped in a reflective foil from **3M** (see figures 4.4 and 4.5). The outer side of this foil is self-adhesive, and this fact made the proper arrangement of the crystals one next to the other quite difficult. Therefore, each wrapped crystal was additionally enveloped in aluminized



Figure 4.7: LYSO *detector*.

Mylar foil. After that, the 3×3 cluster matrix was arranged, and fixed with two holders and long screws. Due to the fact that we have to be able to change the photomultipliers easily, they are not attached to the crystals with silicon glue, but only optically coupled with silicon oil³, and a spring-loaded photomultiplier mount has been developed. That ensures good contact while keeping the photomultipliers detachable. A third plastic piece holds the photomultipliers and voltage dividers. This plastic piece is also attached to the others with long screws. The distance between the plastic holders is determined by steel sleeves surrounding the assembly screws. The figure 4.7 shows a picture of the whole finished detector. The detector is isolated from light with an aluminum foil and put inside a lead cylinder to shield it from background radiation from the beam line.

4.3 Detector positioning

All three detectors have been placed, at least once, behind the interaction region of the Compton backscattering polarimeter for measurement purposes. Since, some times, tests with two detectors have been done, we need a system to put them in the right position in the photon beam. A remote controlled motorized table which can move perpendicularly to the interaction region with the help of a motor was placed on a **MiniTec** structure behind the last dipole magnet. This system permits us to move one as well as the other detector installed on the table into the photon beam. Also measurements to improve the position of each detector have been done.

³ELASTOSIL RT 601 A from **WACKER SILICONES**.

Chapter 5

Measurements

This chapter shows the measurements done with all three detectors as well as comparisons between them. Before the construction of the PbWO_4 detector and the LYSO detector, initial tests were done. Since the BaF_2 detector was already constructed, these tests were not performed with it. Then measurements with radioactive sources were done and also measurements with the electron beam with the detectors in their supposed position in the Compton backscattering polarimeter in order to compare them.

5.1 First tests with the detectors

Three different materials were tested to select which one is the best for the Compton backscattering polarimeter.

The BaF_2 detector was borrowed from TAPS collaboration, and it was supposed to work quite properly, so no further tests were performed.

For the PbWO_4 detector, only old photomultipliers were available, so they had to be tested to select the best ones.

First of all, a dark current test was done. The experimental setup consisted of a light tight box in which the photomultipliers were put inside and connected to the high voltage and signal cables, through connectors in the wall of the light tight box. In this way, the photomultiplier was isolated from light. The signal cable was connected to an analog oscilloscope in order to see how the dark current pulses look like at 800 V and 1200 V. Photographs in each case were done with different oscilloscope trigger levels to be able to compare the different situations later. The figure 5.1(a) shows an example of the dark current pulses. In all cases the dark current pulses were almost the same and the differences between them were not determinant in our decision.

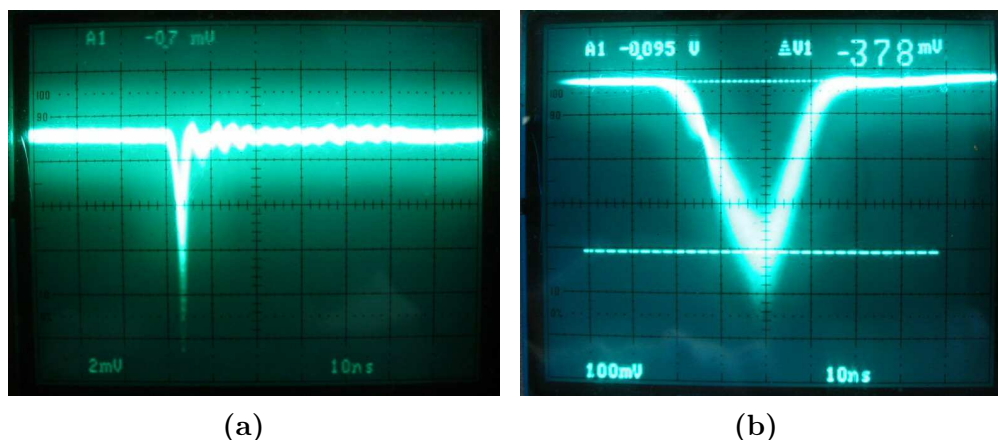


Figure 5.1: *Examples of the dark current (a) pulse and LED (b) pulses.*

After the dark current test, also the amplitude of the signal generated by a LED¹ was measured. The aim was to measure the signal amplitude generated by the same amount of light to select the photomultiplier with highest gain. In this case the photomultipliers were put inside the light tight box, but in front of a LED emitting blue light. The LED was in a fixed position and the photomultipliers were mounted in a support which could be moved in front of the LED. The distance between the LED and the photomultiplier window had to be the same in all cases to reproduce the same conditions. To prove the reproducibility of the measurements, each photomultiplier was located three times in front of the LED and the measurements taken in that conditions showed that the amplitude of the signal, measured in the analog oscilloscope, did not change significantly. The results are shown in the table 5.1.

Also photographs in each case were done and an example of the pulse generated by the LED is shown in the figure 5.1(b).

From the analysis of these photographs and comparing the dark current pulses and the LED pulses the two best photomultipliers to be used with our crystals were extracted. The best one was the **ZH3152** and it was attached to the new PbWO_4 crystal. The old crystal was attached to the **ZH3228**.

A measurement of the gain of the **ZH3152** was done. It was put again into the light tight box and connected to the high voltage. By measuring the charge generated by single photoelectrons at different high voltages, the gain could be calculated. In this case was used a digital oscilloscope which could stop the signal in the screen and had an integration function. The value of the integral at the end of the pulse was measured in $\text{pV}\cdot\text{s}$ and dividing this value by the impedance of the oscilloscope ($50\ \Omega$) one can calculate the deposited

¹Light-Emitting Diode.

PM	Pulse height (mV)
R3478	-86.0
	too less amplification
R6427HA	-378
ZH3228	-384
	-400
R6427HA	-432
ZH3152	-384
	-440
R6427HA	-154
ZH3229	-158
	-161
R6427HA	-305
ZH3172	-312
	-310
R3478	-36.4
	too less amplification

Table 5.1: Test of the photomultipliers with the LED.

Voltage V	Charge (pC)	Gain·10 ⁶
1300	0.43 ± 0.09	(2.7 ± 0.6)
1400	0.50 ± 0.06	(3.1 ± 0.4)
1500	1.13 ± 0.11	(7.3 ± 0.7)
1600	1.0 ± 0.2	(6.3 ± 1.3)
1700	1.5 ± 0.2	(9.1 ± 1.3)
1800	2.12 ± 0.05	(13.3 ± 0.3)
1900	1.92 ± 0.11	(12.0 ± 0.7)
2000	6.0 ± 0.9	(37.5 ± 0.6)

Table 5.2: Measurement of the gain of the photomultipliers by using the single photoelectron charge deposition.

charge in pC. The measured values which are represented in the table 5.2 are the mean values of three measurements and their standard deviation was taken as the error.

The difficulty of this method was to select which of the pulses were related with single photoelectrons. The pulses on the oscilloscope screen have different sizes. The smallest pulses were supposed to come from single photoelectrons. Other pulses larger than these, which were approximately two and three times bigger, were supposed to come from two and three photoelectrons

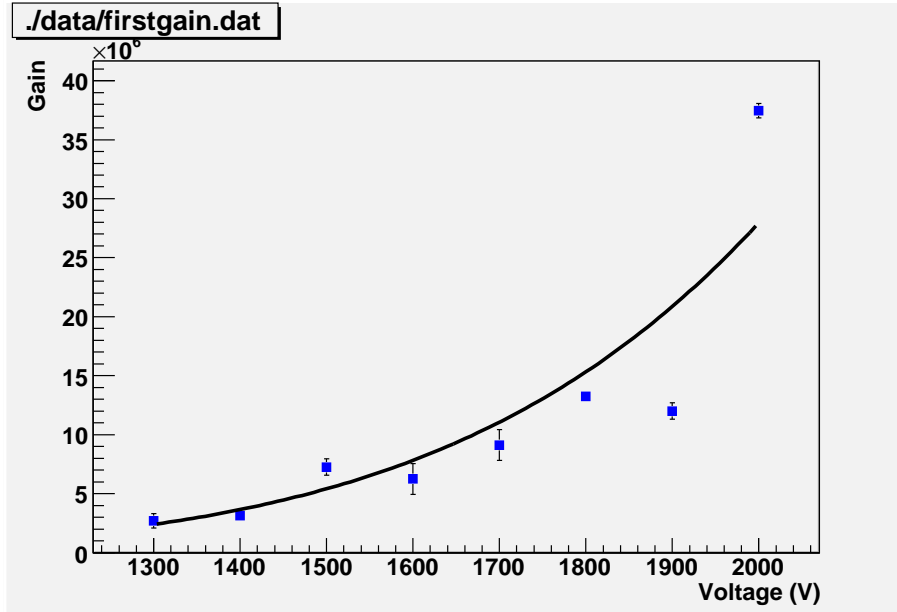


Figure 5.2: Estimation of the gain of the photomultiplier *ZH3152*.

emitted roughly at the same time.

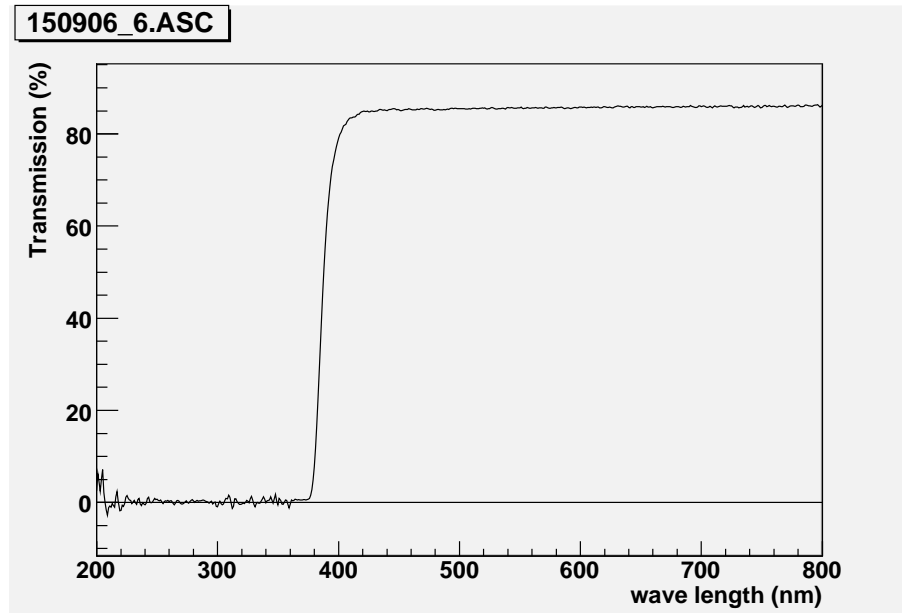
The problem with the smallest pulses is that they could be generated also by electrons emitted in the intermediate stages. There is no way to know exactly whether the pulses on the oscilloscope screen were generated by a single photoelectron or by an electron from one of the intermediate dynodes, but we can select those which could be related with single photoelectrons with most probability. This is not yet a problem at lower voltages (below about 1800 V in our case), but at higher voltages, pulses smaller than those supposed to come from single photoelectrons occur. Therefore the error increases substantially.

The law which describes the multiplication of the electrons in the photomultiplier, taking into account the secondary emission in the dynodes, has the form (see [MF02]):

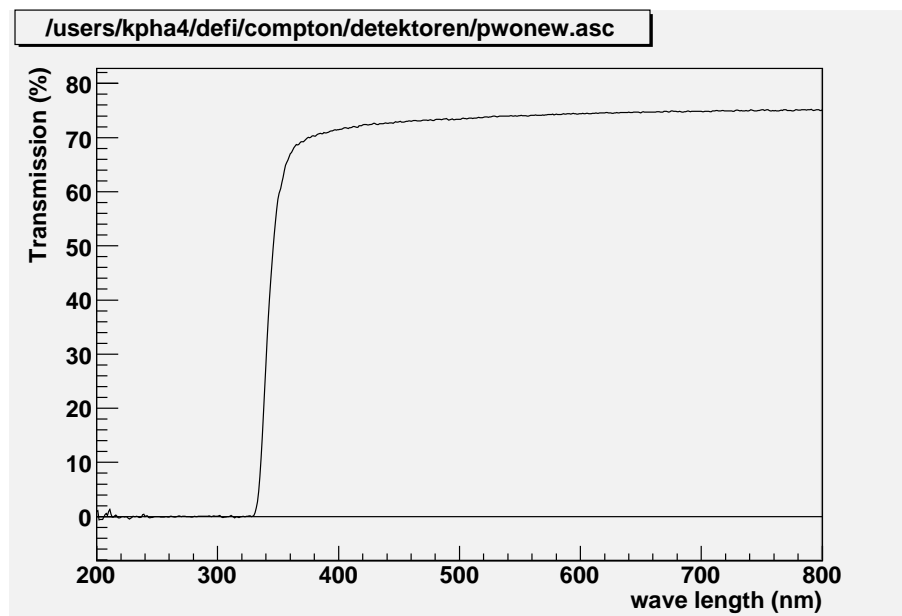
$$y = a \cdot x^b \quad (5.1)$$

where y is related to the charge and x to the Voltage.

The result of a fit with this function is $y = [(4.0 \pm 0.8) \cdot 10^{-12}] \cdot x^{(5.71 \pm 0.02)}$. If one compares the result of the fit with the data from the data sheet of the photomultiplier, we can say that the photomultiplier works still properly (see the figure 5.2). For a voltage of 1300 V the data sheet shows a gain of $2 \cdot 10^6$, for 1500 V a gain of $5 \cdot 10^6$ and a gain of $8 \cdot 10^6$ at 1600 V, which are almost



(a)



(b)

Figure 5.3: Transmission spectra for LYSO (a) and PbWO_4 (b).

the same values that one can extract from the fit curve.

The next test which was done was the measurement of the transmission of the crystals using a spectrophotometer in the UV and visible range from **SHIMADZU**, model **MPC-3100**. The measured spectra can be seen in figure 5.3 for the new PbWO_4 crystal and one of the LYSO crystals.

Both spectra are similar and the principal conclusions which can be extracted are that the crystals have no transparency for wavelengths up to about 400 nm, and transmit almost 85% of the light from this wavelength on in the case of LYSO and around 74% of transmission in the case of PbWO_4 from the same wavelength on. Taking into account the refractive indexes of both materials and using the Fresnel equations, the theoretical values of transmitted light are exactly 85% for LYSO and 74% for PbWO_4 . The wavelength emission maximum for both crystals is around 420 nm, so this is consistent with their characteristics.

5.2 Measurements with radioactive sources

Measurements of the spectra of different radioactive sources permit to perform an energy calibration as well as calculate the energy resolution of the different materials. The energy calibration gives also an idea of the linearity of the detector and the photomultipliers.

PbWO_4

For PbWO_4 , spectra were taken at room temperature and at -25°C .

Due to the very low light yield of this material, the different peaks of radioactive sources are not well resolved. Measurements with ^{60}Co at different HV are shown in the figure 5.4. The first peak in all spectra is the pedestal generated by a clock with known frequency which triggers the ADC read out. At 1200 V and 1500 V the ^{60}Co lines were not enough amplified, they were under the discrimination threshold or next to the pedestal. At 1800 V one can start to see a peak, but very broad and the two lines can not be resolved.

Also muons from the cosmic radiation were measured (Figure 5.5). Since the muons deposit much more energy (in our case if they hit the detector perpendicularly approximately 20.04 MeV) than photons coming from radioactive samples, with the same HV as the measurements taken with ^{60}Co ,

²⁶⁰Co decays emitting two photons with energies 1.17 MeV and 1.33 MeV

5.2 Measurements with radioactive sources

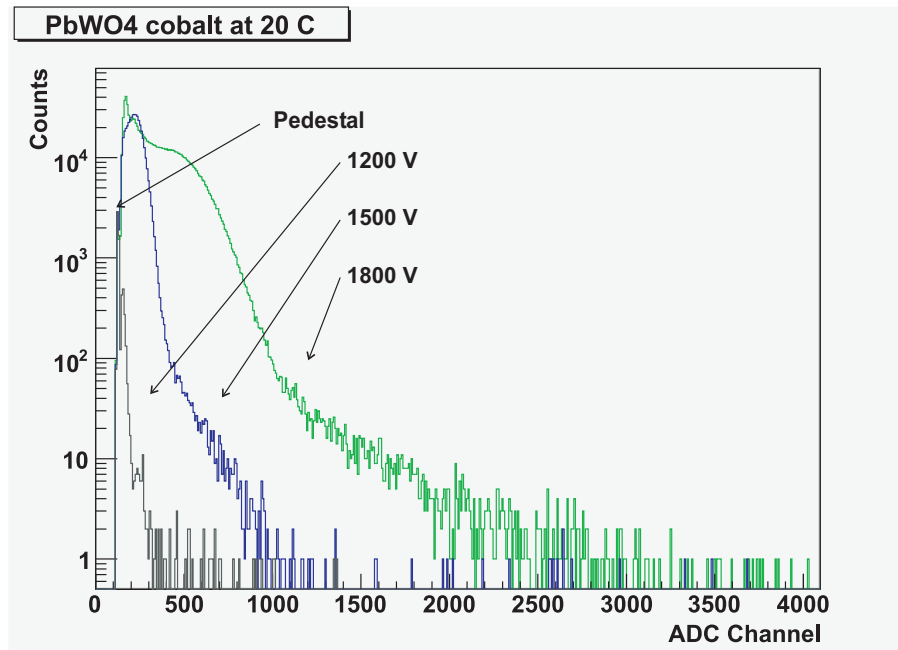


Figure 5.4: ⁶⁰Co spectra measured with PbWO₄ at room temperature. **Grey:** HV at 1200 V; **Blue:** HV at 1500 V; **Green:** HV at 1800V.

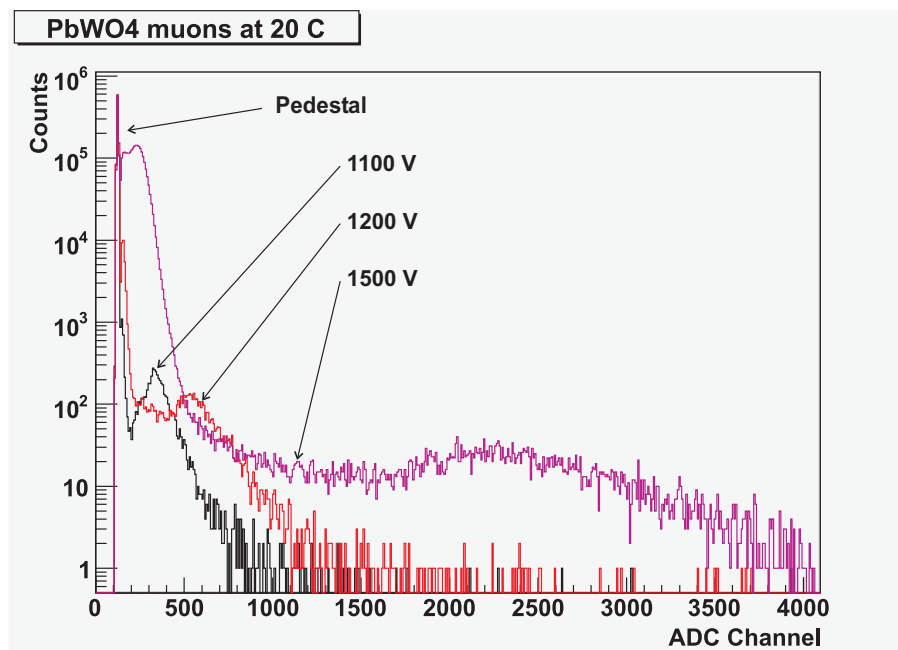


Figure 5.5: Muon spectra measured with PbWO₄ at room temperature. **Black:** HV at 1100 V; **Red:** HV at 1200 V; **Pink:** HV at 1500V.

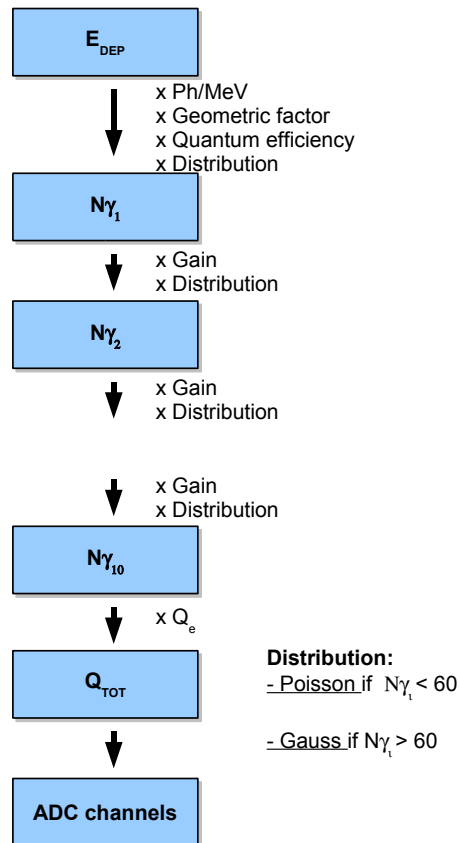


Figure 5.6: ^{60}Co lines and muons simulation. The input values were the energies deposited by ^{60}Co photons or muons respectively, and the parameters which have been used in the simulation were the light yield of the PbWO_4 at room temperature, an estimated value of the quantum efficiency of the photomultiplier photocathode and an estimation of a geometric factor of the crystal. The multiplication of the electrons in each of the dynodes of the photomultipliers was calculated using the Poisson distribution in the first stages and a Gaussian distribution in the others.

we can see the peak in the spectra. Nevertheless, we did not have good energy resolution. Since the spectra taken with radioactive sources or muons were not very clear, a simple spectra simulation was done to see whether our spectra were as expected or not. This simulation was programmed in a ROOT³ script. The input values were the energies deposited by muons or ⁶⁰Co photons respectively, and the parameters which have been used in the simulation were the light yield of the PbWO₄ at room temperature, an estimated value of the quantum efficiency of the photomultiplier photocathode and an estimation of a geometric factor of the crystal. In the figure 5.6 one can see a scheme of the simulation.

The number of photons generated in the crystal was estimated using the mean value of photons generated per MeV and the Poisson distribution. The number of photoelectrons which are generated at the photocathode can be calculated using the quantum efficiency and the geometric factor of the crystal. The multiplication of the electrons in each of the dynodes of the photomultipliers was calculated using the Poisson distribution in the first stages and a Gaussian distribution in the others, taking into account how many electrons had been generated until this moment. Knowing the amount of charge per ADC channel⁴, we can fill a histogram with the events. The results of this simulation for the ⁶⁰Co lines (1.17 and 1.33 MeV respectively) and perpendicularly incident muons in the crystal (20.04 MeV) are shown in the figure 5.7.

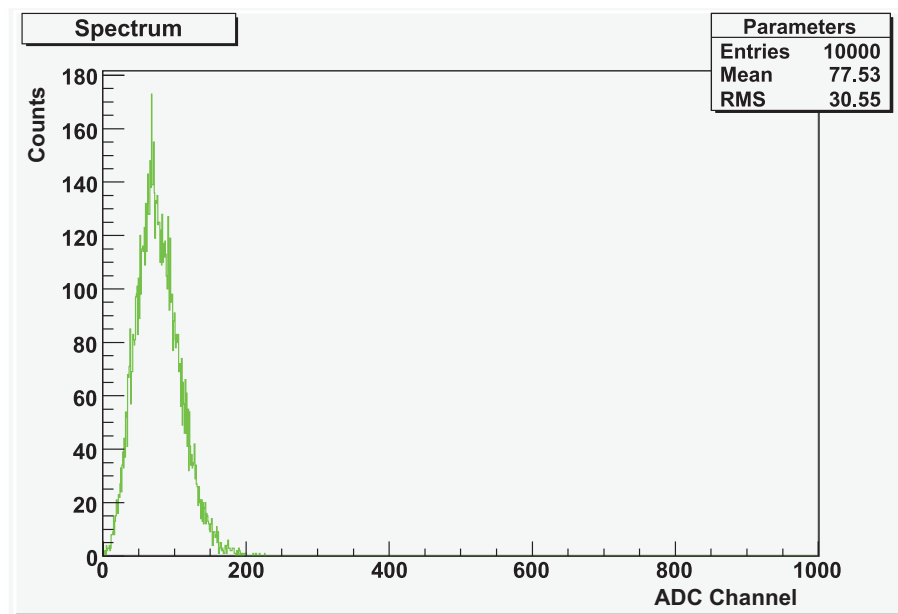
In the simulation of the ⁶⁰Co lines at 1500 V (Figure 5.7(a)), the two peaks are not well resolved and they lie around the channel 75. In the real spectrum taken with ⁶⁰Co, around this channel over the pedestal these lines could not be seen, but they start to appear in the spectra. The width of the peak in the real data can not be estimated because of the large background that it can not be separated from.

In the muon simulation the situation is almost the same (Figure 5.7(b)). The peak appears around the channel number 400 as in the real spectrum at 1200 V. Nevertheless in the measured spectra the peak is broader because in the simulation only the energy deposition of the muons which hit the detector perpendicularly have been taken in account.

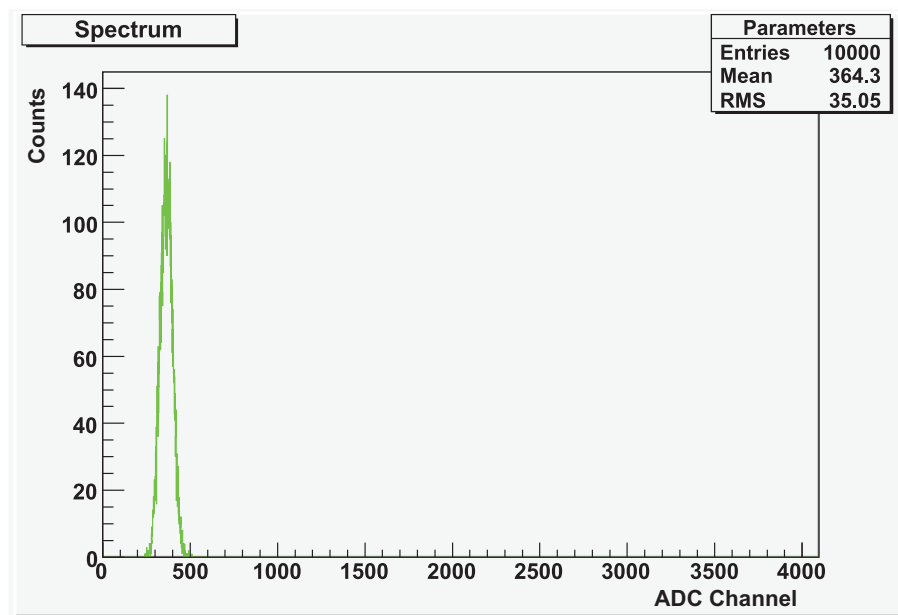
After the first measurements the detector was cooled down to -25°C during the beam time. At such temperatures, the detector was supposed to have much more light yield. Also measurements with radioactive sources and with muons were done under these conditions. We can see the spectra of ⁶⁰Co and muons respectively in the figures 5.8 and 5.9. Effectively, one

³<http://root.cern.ch/>

⁴In our case, the ADC has 4096 channels, and the maximum charge which can be digitized is 800 pC. That means that each ADC channel represents approximately 0.20 pC



(a) ^{60}Co 1500 V



(b) Muons 1200 V

Figure 5.7: Spectra simulation for the PbWO_4 : (a) ^{60}Co at room temperature and 1500V; (b) Muons at room temperature and 1200V.

5.2 Measurements with radioactive sources

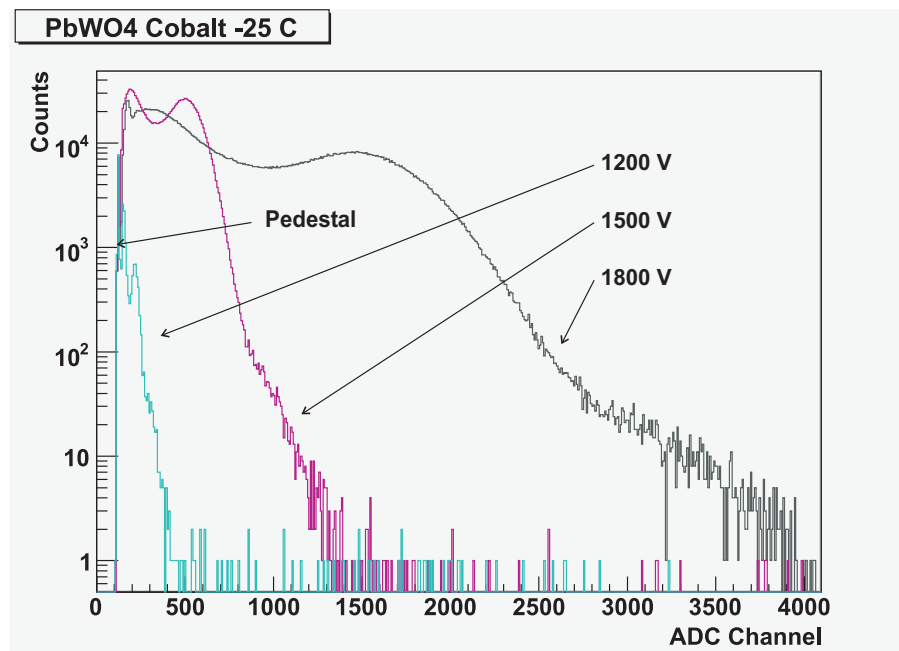


Figure 5.8: ^{60}Co spectra measured with PbWO_4 at -25°C . **Blue:** HV at 1200 V; **Pink:** HV at 1500 V; **Grey:** HV at 1800 V.

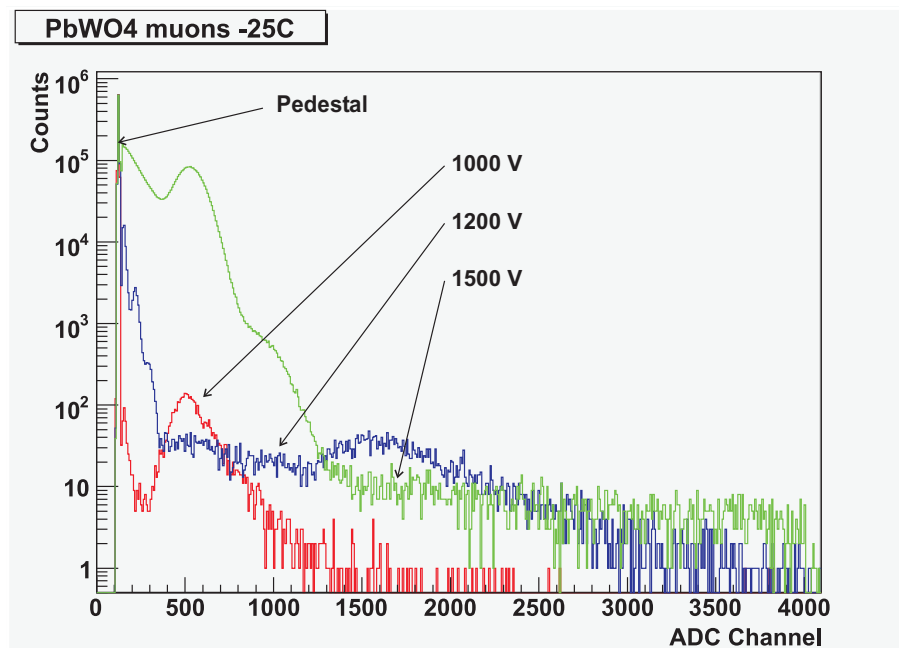


Figure 5.9: Muon spectra measured with PbWO_4 at -25°C . **Red:** HV at 1000 V; **Blue:** HV at 1200 V; **Green:** HV at 1500 V.

factor of approximately 3 as expected [B⁺07].

In the figures 5.10 and 5.11 one can compare the spectra of an AmBe⁵ source taken at room temperature and at -25 °C at different voltages. Measurements of a ¹³⁷Cs source showed no peak, even at low temperatures. The conclusion is that this detector had not enough energy resolution and too low signal due to the light yield.

BaF₂

Spectrum measurements of several radioactive sources taken with the BaF₂ detector are shown in figure 5.12. Only by having a look to the spectra, one can easily see that this detector has better energy resolution than PbWO₄. The structures of the spectra for the different sources are recognizable.

The red line in figure 5.12(a) represents the ⁶⁰Co spectrum and the grey is background. The two recognizable peaks in the background spectrum come from intrinsic radioactivity in the BaF₂ [Sch89]. The peak shown in the ⁶⁰Co spectrum comes from the 1.33 MeV and 1.17 MeV decay lines, but unresolved.

The figure 5.12(b) shows the spectra of ¹³⁷Cs⁶ (blue) and ²²Na⁷ (grey). One can see the two peaks coming from background and the 0.662 MeV peak from the ¹³⁷Cs decay as well as the annihilation peak (0.511 MeV) and photopeak (1.27 MeV) from the ²²Na.

Finally, in the figure 5.12(c) background and ²²⁸Th⁸ spectra are represented. Both are very similar due to the low activity of the ²²⁸Th source. The 2.62 MeV peak from the ²²⁸Th decay can be suspected between the two background peaks.

To perform the energy calibration of this detector, the positions of the different peaks of the spectra were measured using a Gaussian fit. The value of the χ^2/ν of the Gaussian fit was too large in almost all cases, due to the fact that the peaks are not exactly represented by a Gaussian function.

⁵This source contains an alloy of ²⁴¹Am and ⁹Be. The α -particles from the decay of ²⁴¹Am are absorbed by the ⁹Be, forming a ¹³C compound nucleus that emits a neutron turning in ¹²C*. This excited state decays into the ¹²C ground state by emission of a photon with an energy of 4.43 MeV.

⁶¹³⁷Cs decays via β^- into the ¹³⁷Ba* which decays to the ground state emitting one photon with 0.662 MeV

⁷²²Na decays via β^+ into the ²²Ne*, one can see in the spectra the annihilation peak, with 0.511 MeV and the photopeak from the ²²Ne* decay with 1.27 MeV

⁸²²⁸Th decays into unstable isotopes creating a radioactive chain. The last decay comes from the ²⁰⁶Pb* and has a peak of 2.62 MeV

5.2 Measurements with radioactive sources

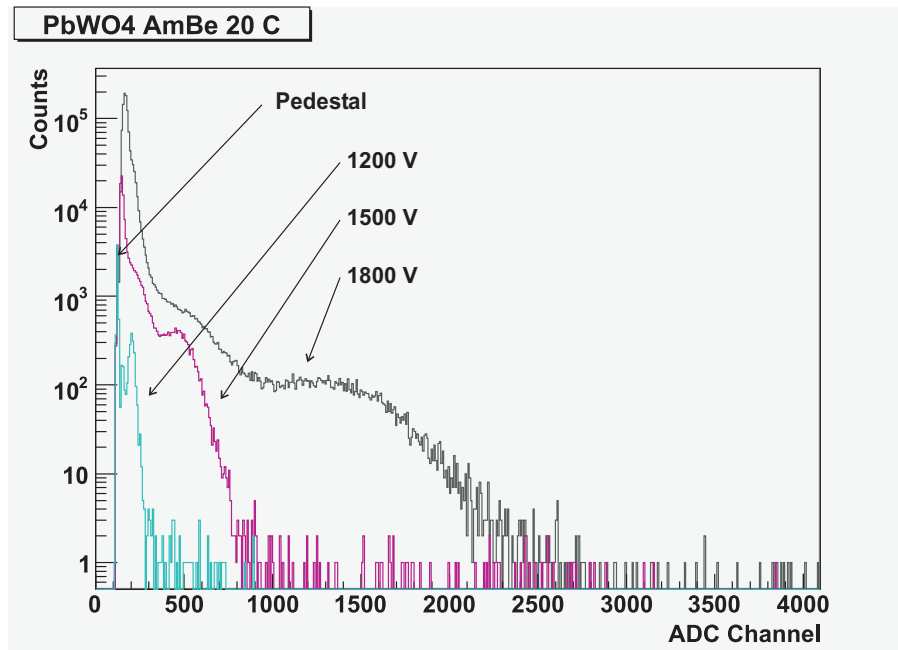


Figure 5.10: AmBe spectra measured with PbWO_4 at room temperature. *Blue:* HV at 1200 V; *Pink:* HV at 1500 V; *Grey:* HV at 1800 V.

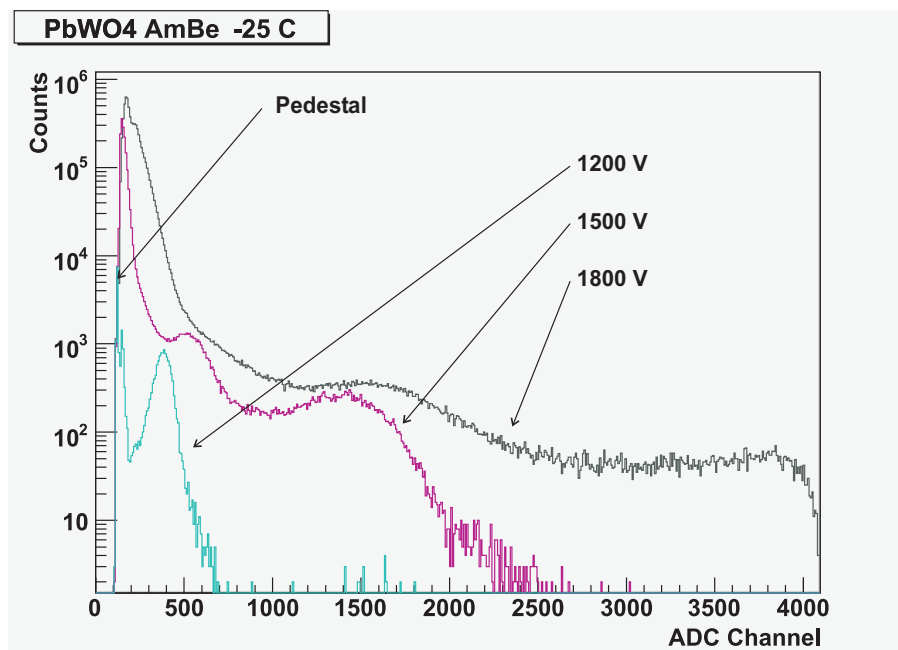
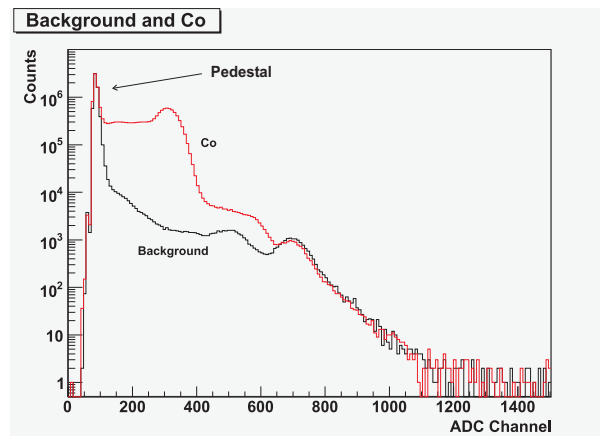
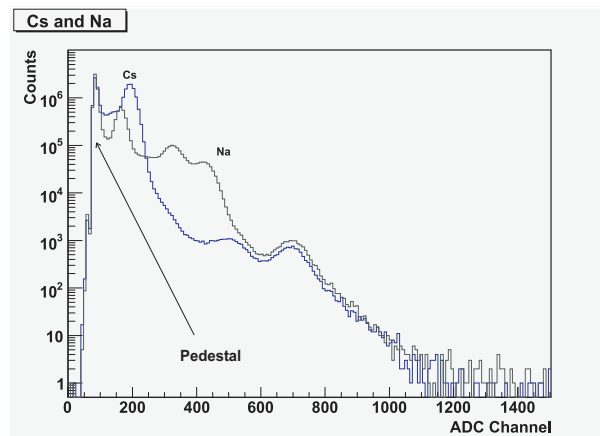


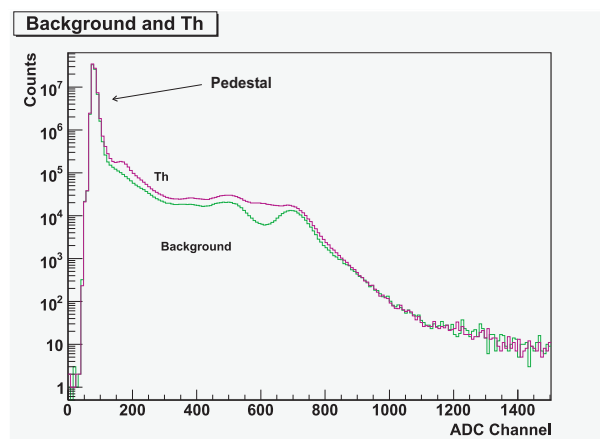
Figure 5.11: AmBe spectra measured with PbWO_4 at -25°C . *Blue:* HV at 1000 V; *Pink:* HV at 1200 V; *Grey:* HV at 1500 V.



(a) Grey: Background; Red: ^{60}Co .



(b) Blue: ^{137}Cs ; Grey: ^{22}Na .



(c) Green: Background; Pink: ^{228}Th .

Figure 5.12: Spectra with BaF_2 . (a) Background and ^{60}Co ; (b) ^{137}Cs and ^{22}Na ; (c) Background and ^{228}Th .

5.2 Measurements with radioactive sources

However, a fit trying to fit the background or subtracting it from the spectra was extremely difficult. On the other hand, small variations in the applied voltage, due to the instability of the power supply and variations in the temperature, produced variations in the position of the peak which are not represented by the statistical errors of the peak parameters. A first energy calibration was done using the values from the Gaussian fits and their errors, and a linear fit was quite good except for the χ^2/ν value, which was too large. Using a second degree polynomial the third parameter was around 6 orders of magnitude less than the others. That showed that the too large χ^2/ν value is mainly due to the underestimated errors and not due to a non-linearity of the detector system. In order to estimate better errors the value of the χ^2/ν of this fit was used. Using this formula [BR03]:

$$\sigma_i'^2 = \sigma_i^2 \cdot \chi^2/\nu \quad (5.2)$$

one can estimate the new errors for the fit, where $\sigma_i'^2$ are the new estimated errors and σ_i^2 are the old errors. i represents each point in the plot.

The fit for the energy calibration of the BaF₂ with the spectra measured at HV = 1850 V shows a good linearity (Figure 5.13) and the results for the χ^2/ν are satisfactory, in this case $\chi^2/\nu = 0.953$.

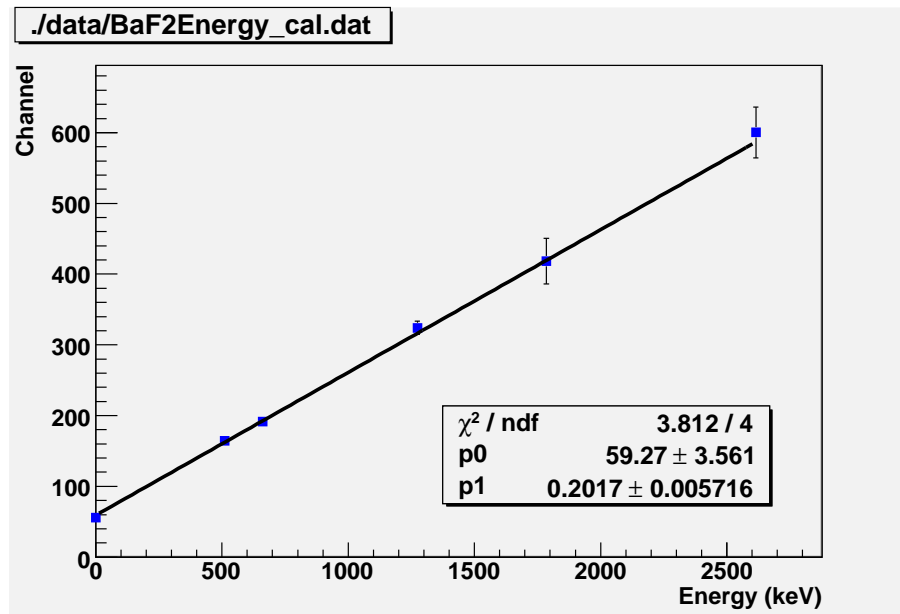


Figure 5.13: BaF₂ energy calibration.

Trying to perform a fit using a second degree polynomial the value of the $\chi^2/\nu = 1.236$, which was too large and the third parameter of the fit

Chapter 5. Measurements

was again six orders of magnitude less than the others. The linearity of the detector can be considered to be good.

From the measurements of the peak positions and their widths we can also calculate the energy resolution. It is defined as:

$$R_E = \frac{\Delta E}{E} = \frac{FWHM}{\mu} \quad (5.3)$$

where $FWHM$ is the width of the peak at its half height and μ is the mean value of the peak, corrected from the pedestal position. It is related with the width σ of the Gaussian distribution as follows:

$$R_E = \frac{2.35\sigma}{\mu} \quad (5.4)$$

Notice that this is a dimensionless value, and it can be calculated using channels as well as energies.

At 1850 V the measured energy resolution of the BaF₂ for different energy depositions (peaks) is shown in the table 5.3.

E_γ (keV)	R_E (%)
511	34.20 ± 0.02
662	30.471 ± 0.010
1275	29.46 ± 0.12

Table 5.3: *Energy resolution for BaF₂*

The values calculated by the TAPS collaboration are represented in the table 5.4. As one can see, we don't achieve the same energy resolution as the TAPS collaboration. It is consistent with what we see in our spectra. We can not resolve the two ⁶⁰Co lines.

E_γ (keV)	R_E (%)
662	15.5 ± 0.4
1173	14.4 ± 0.3
1333	11.1 ± 0.2
2505	8.1 ± 0.2

Table 5.4: *Energy resolution of BaF₂ calculated by TAPS collaboration [Sch89].*

LYSO

Also spectrum measurements with different radioactive sources were taken with the LYSO crystals. The figure 5.14 shows the spectra taken with the

5.2 Measurements with radioactive sources

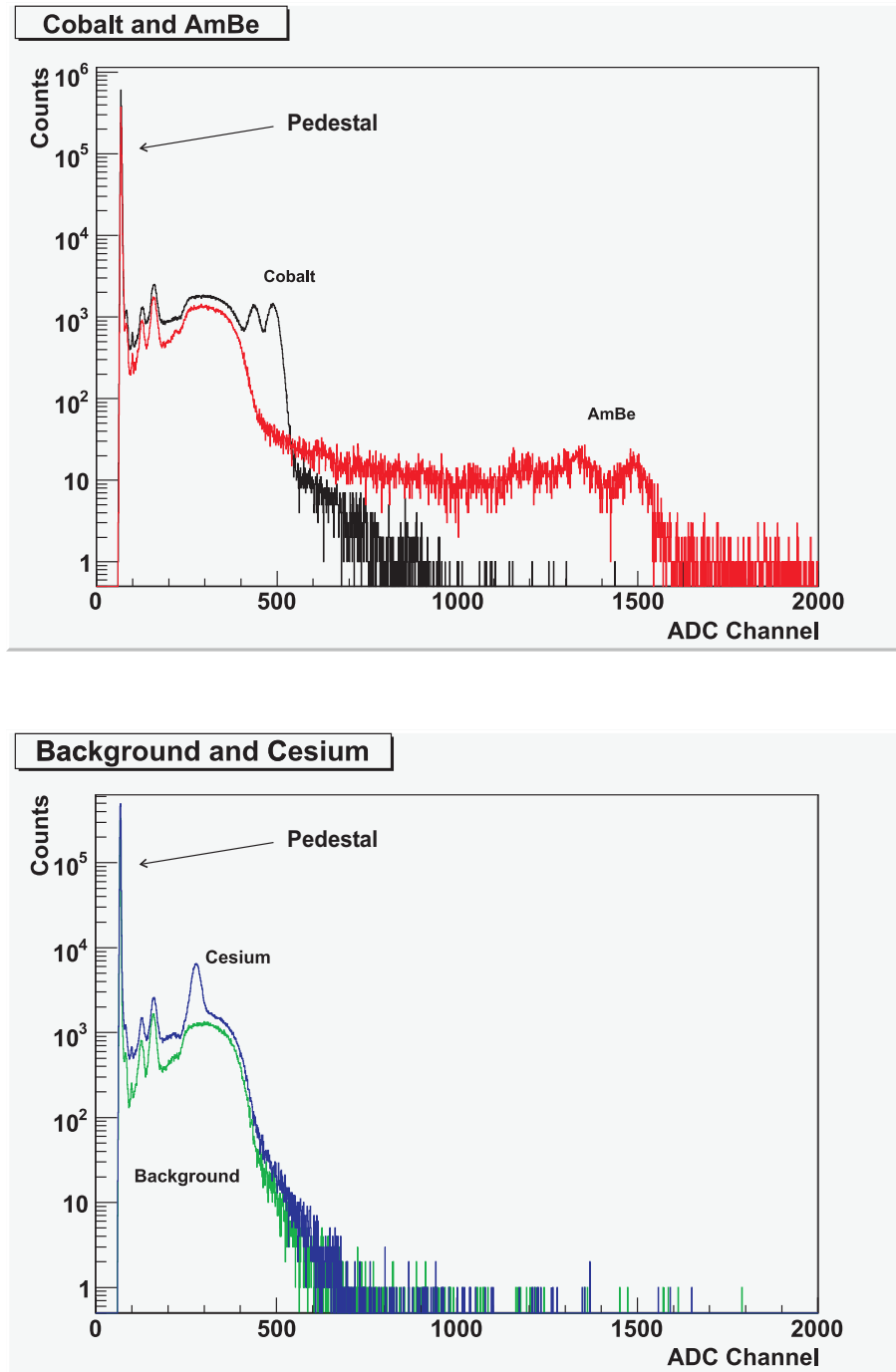


Figure 5.14: Spectra taken with LYSO central crystal. Top: AmBe (Red) and ⁶⁰Co (Black) source; Bottom: ¹³⁷Cs (Blue) and Background (Green).

Chapter 5. Measurements

LYSO central crystal.

As in the spectra measured with the BaF₂ and the PbWO₄, we can see the pedestal in first place next to zero. Then two small peaks and a continuous spectrum coming from the β decay of ¹⁷⁶Lu in the LYSO itself. From the decay of ¹⁷⁶Lu, we have three peaks from gammas with energies 306 keV, 202 keV and 88 keV. The line with 88 keV is very close to the pedestal and can not be clearly seen in all spectra.

The figure 5.15 shows the spectra of different radioactive sources taken with the whole detector, i. e. with the sum of the nine crystals. In this case the three lines from the intrinsic radioactivity of the crystal are summed to the beta spectrum. Therefore, we see from the intrinsic radioactivity the beta spectrum shifted by the sum of the gamma lines.

These spectra are the best which have been taken with different detectors since the two lines of the ⁶⁰Co are well resolved.

From these spectra we have also performed an energy calibration for the LYSO crystals. In this calibration, also the peaks coming from the intrinsic radioactivity of ¹⁷⁶Lu have been taken into account. The same problem with the errors as with the BaF₂ occurred and it was treated in the same way. The results of the fits are shown in the figures 5.16 and 5.17. The values of the χ^2/ν were 0.999 and 1.002 respectively.

Crystal N.	R_E at	
	1.33 MeV	1.17 MeV
Sum	16.00 ± 0.06	23.37 ± 0.06
1	9.11 ± 0.14	11.0 ± 0.4
2	8.87 ± 0.10	10.0 ± 0.3
3	9.10 ± 0.13	12.0 ± 0.4
4	8.79 ± 0.10	11.7 ± 0.2
5	9.8 ± 0.10	12.2 ± 0.2
6	9.34 ± 0.10	11.3 ± 0.3
7	8.68 ± 0.10	11.3 ± 0.3
8	8.82 ± 0.12	11.2 ± 0.2
9	9.66 ± 0.11	12.2 ± 0.3

Table 5.5: Energy resolution for LYSO.

The calculated energy resolution for the LYSO using the ⁶⁰Co lines is shown in table 5.5.

In the data sheet from **Saint Gobain** the expected value for the energy resolution of this material is approximately 7% for photons of 0.662 MeV measured with a crystal of 30 mm of diameter and 15 cm long. The energy

5.2 Measurements with radioactive sources

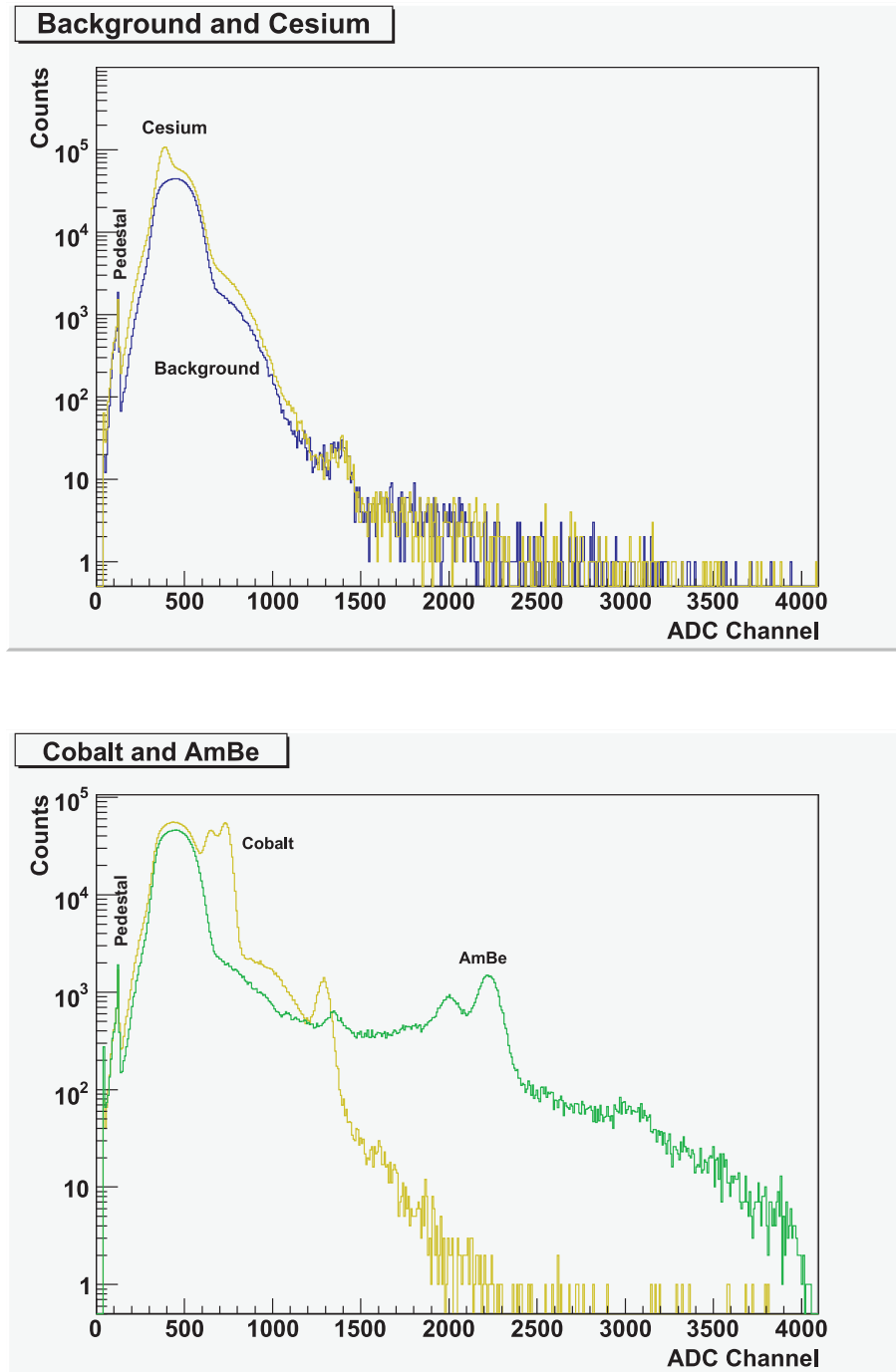


Figure 5.15: *Radioactive spectra taken with fullLYSO detector. Top: Background (Blue) and ^{137}Cs (Yellow). Bottom: ^{60}Co and AmBe (Green).*

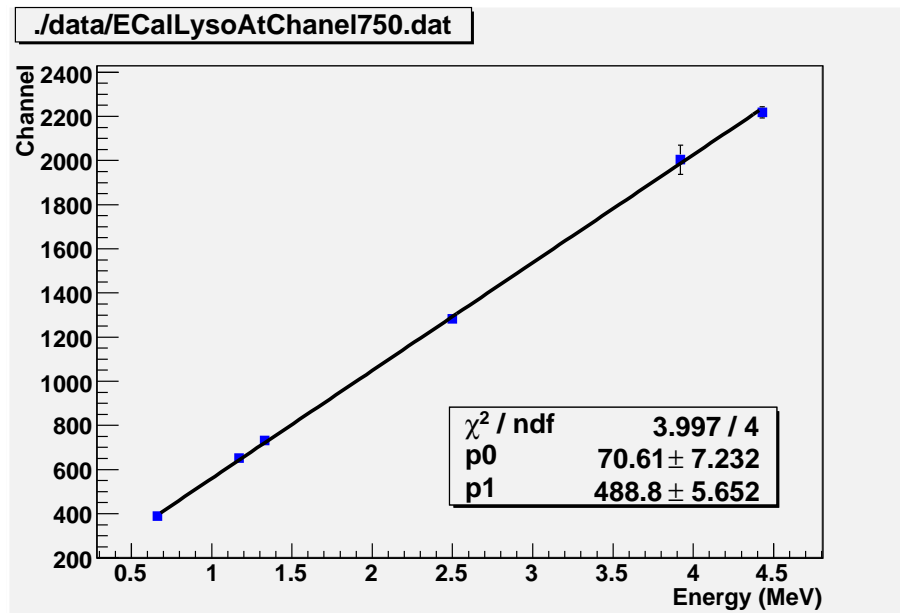


Figure 5.16: LYSO energy calibration.

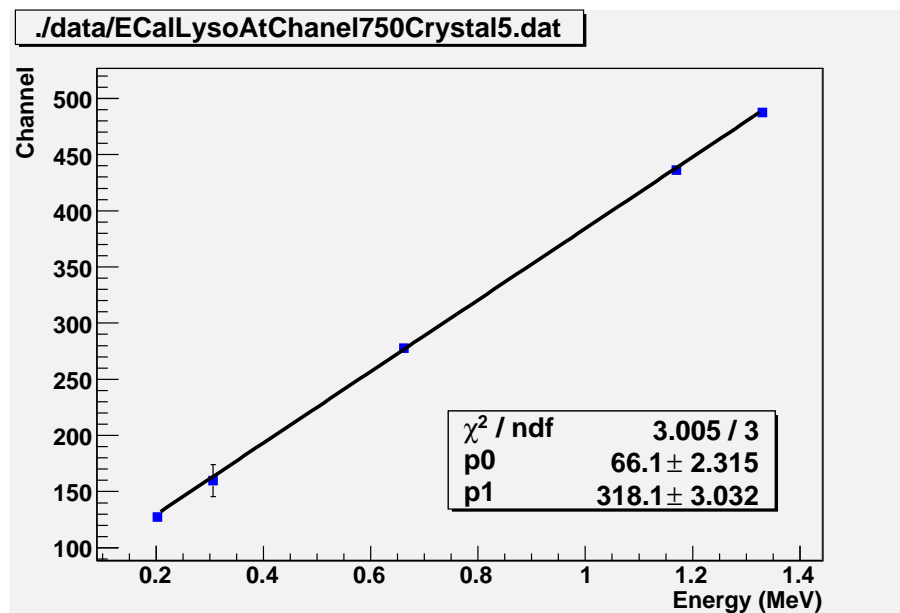


Figure 5.17: LYSO energy calibration only for the central crystal.

resolution can be considered good but not as good as the expected values.

5.3 ADC tests

When measurements with BaF₂ were being taken, a problem with the pedestal in the ADC was found. Its position changed in spectra taken under the same conditions and the number of counts which it contained was not consistent with the pedestal clock frequency.

Att (dB)	0	1	2	3	4	5	6	7
Charge(pC)	120	107.6	96	85.61	76.32	68.33	60.85	54.42
Att (dB)		8	9	10	12	15	20	21
Charge(pC)		48.71	43.45	38.77	30.95	21.34	12	6.74

Table 5.6: *Attenuation.*

The origin of the problem was found in the transformers which were put between the analog signal cables and the ADC inputs. After removing the transformers the pedestal position and rates were consistent with our expectations.

In order to prove the right position of the pedestal and the linearity of the ADC one test with one pulser was done.

The signal of a **LeCroy Instapulser** which generates pulses of 120 pC was connected to an attenuator and from this to each signal cable of the LYSO detector, as well as to the signal sum cable, one to one.

Then a spectrum for each channel was taken changing the attenuation of the signal.

For each attenuation we know which is the amount of charge which is sent to the ADC by knowing the definition of dB

$$G = 20 \cdot \log \frac{I_{out}}{I_{in}} \quad (5.5)$$

But the current is defined as follows:

$$I = \frac{dQ}{dt} \quad (5.6)$$

and substituting 5.6 in 5.5 we obtain

$$G = 20 \cdot \log \frac{Q_{out}}{Q_{in}} \quad (5.7)$$

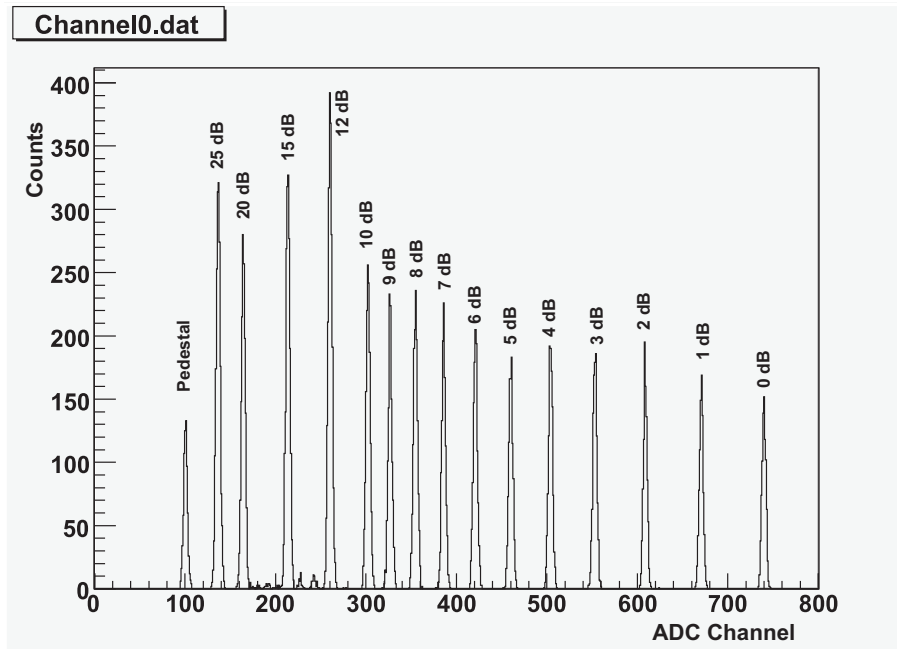


Figure 5.18: Pulser spectrum taken with the ADC by attenuating the pulser input charge.

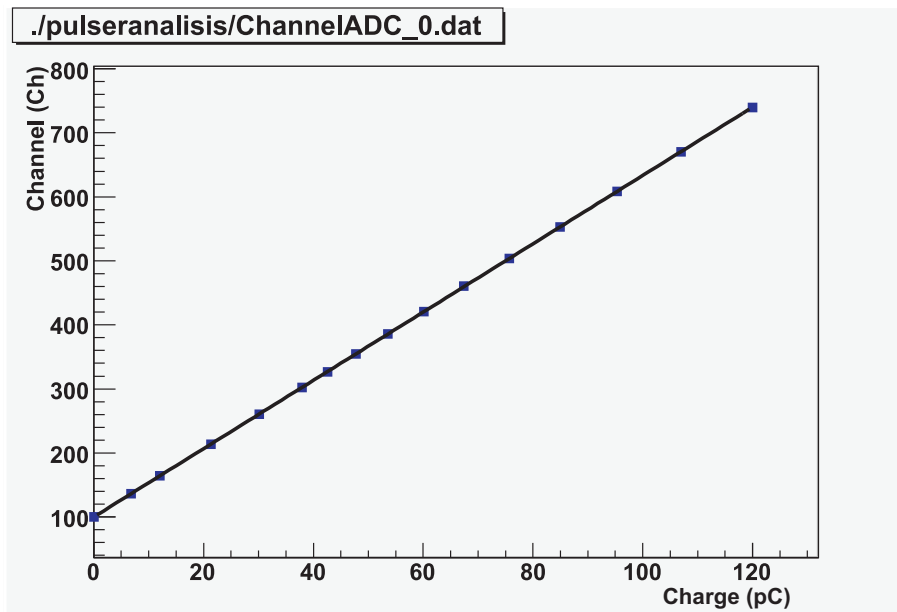


Figure 5.19: Test with pulser fit result.

where G represents the attenuation factor.

The corresponding charge to each attenuation factor is calculated in the table 5.6.

As an example of the spectra taken with the pulser, one can see the figure 5.18, which corresponds to the input channel number 0 to the ADC. One can see in this spectrum from left to right the pedestal and the peaks related with 25 dB, 20 dB, 15 dB, 12 dB, 10 dB, 9 dB, 8 dB, 7 dB, 6 dB, 5 dB, 4 dB, 3 dB, 2 dB, 1 dB and 0 dB of attenuation. By measuring the peak positions in these spectra and representing them versus its corresponding amount of charge, we can see whether the ADC is linear or not and prove that the pedestal position is right. As an example the fit for the input channel 0 of the ADC is shown in figure 5.19. As one can see, the pedestal position corresponds to zero charge as it should and the linearity is also satisfactory.

5.4 Measurements with the beam

Before taking measurements with the detectors in the Compton polarimeter experimental setup, that is with the electron beam on, a delay scan be-

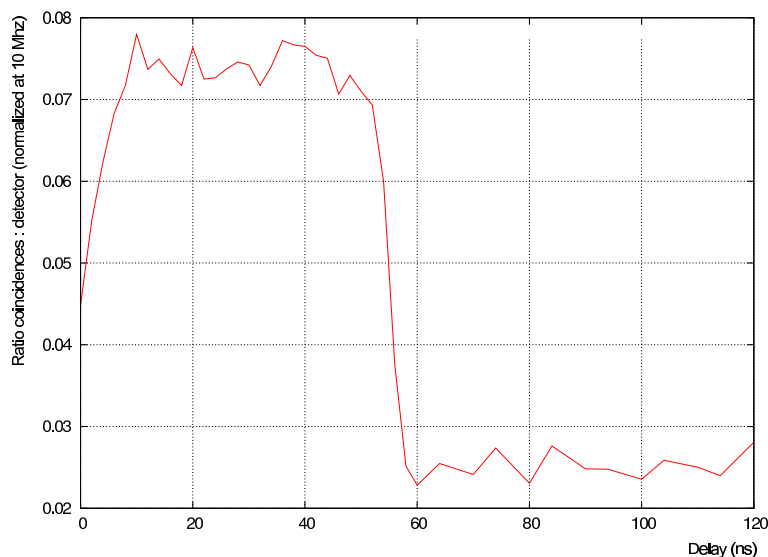


Figure 5.20: *Delay curve between the electron and photon detectors.*

tween fibre and photon detectors was performed. It is shown in the figure 5.20. The relative delay between fibre and photon detectors can be changed gradually from 0 to 120 ns (see figure 3.12 in the chapter 3). For each delay one can measure the coincidence rate. In the figure 5.20 the coincidence rate

normalized to the rate in the photon detector is shown for each delay value. The values of the rates for each run have also been previously normalized using a 1 MHz clock. As one can see, the optimal delay to have both detectors in coincidence is in this case 30 ns and 120 ns to have them out of coincidence. The coincidence rate for delays above 60 ns arises from accidental coincidences which can be derived from:

$$\dot{N}_{acc} = \dot{N}_{\gamma} \cdot \dot{N}_e \cdot (\tau_{\gamma} + \tau_e) \quad (5.8)$$

where τ_{γ} is the pulse width from the photon detector at the coincidence input, τ_e the pulse width of the electron detector at the coincidence input and \dot{N}_{γ} and \dot{N}_e are the rates of the detectors.

In this case we can see a normalized accidental coincidence rate of approximately 0.025. From the formula 5.8 the expected value of the accidental coincidences is about 0.019. The number of accidental coincidences is about a 32% higher than expected. Since the quality of the beam at that time was quite bad, the rates in the fibre detector were very high. The enlargement of the accidental coincidences can be explained by the time resolution of the electronics, which is insufficient to hold this high rates. The pulses of subsequent events can overlap creating long pulses which look to the coincidence unit like a longer gate while they are counted as one event by the scaler. Therefore the τ_e is effectively increased, while the rates are underestimated.

Also since the photon detectors can be moved horizontally behind the interaction region, a position scan was performed. The results of this were not determinant. Spectra were taken moving the detector in steps of 2 mm out of the beam line in both right and left directions. Around the beam line, to place the detector 2 mm to the right or to the left does not show significant changes in the spectra. The precision we can reach when aligning the detector on the beamline is about ± 2 mm.

After these first settings, measurements with several different conditions could be done.

5.4.1 Different fibres in trigger

One of the first tests which was done with all three detectors is to measure bremsstrahlung photons in correlation with electrons which hit the fibre detector.

Taking into account the delay between both detectors, one can measure with the fibres in coincidence with the photon detector or not, by changing the relative programmable delay as the delay curve describes. With these

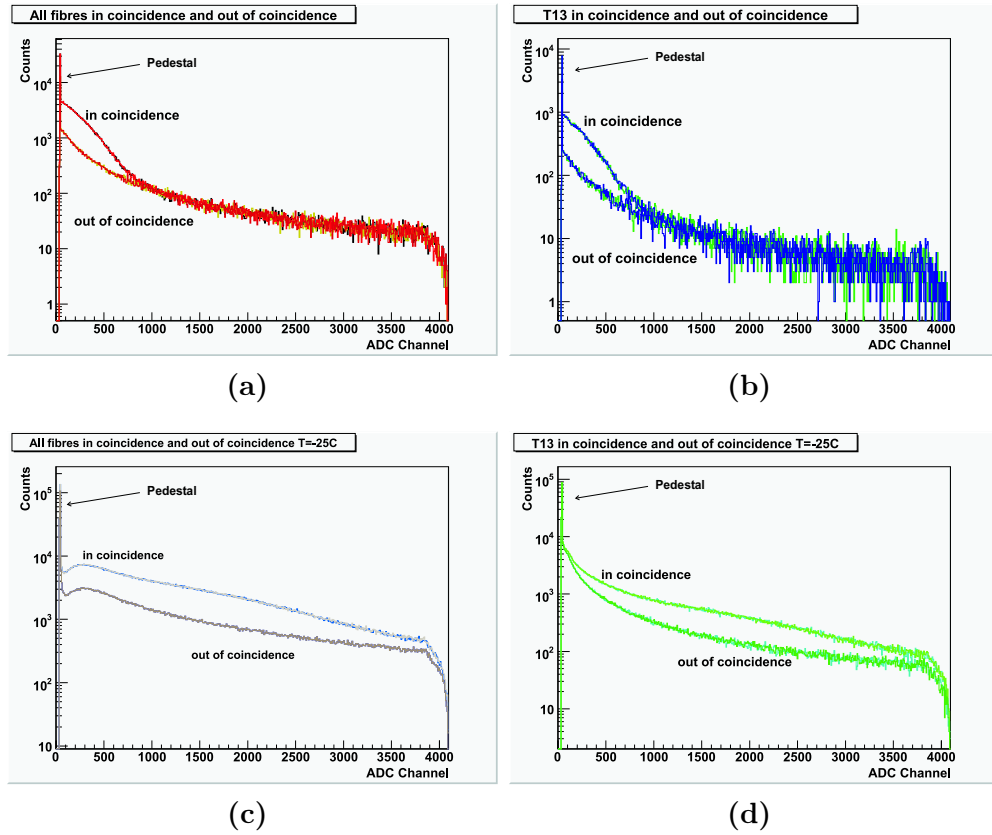


Figure 5.21: PbWO_4 spectra at different temperatures: (a) All fibres in coincidence at room temperature; (b) T13 in coincidence at room temperature; (c) all fibres in coincidence at -25°C ; (d) T13 in coincidence at -25°C .

assumptions, spectra were taken with the PbWO_4 detector at different temperatures in order to measure the amplitude of the signal and notice the increase of the light yield. In figure 5.21 one can see spectra of some of these measurements enabling all the fibres or only one trigger channel (in this case T13) and in each histogram with both detectors in coincidence and out of coincidence. Out of coincidence we only can have an estimation of the accidental coincidences, which can be subtracted from the coincidence spectrum. One can see in the figure 5.21 that above the acceptance range of T13 (e. g. 5.21(b) above the channel 1000) only accidental coincidences can occur. Notice that each histogram contains lines in two colors, which correspond to the positive or negative helicity of the electron beam.

The figures 5.21(a) and 5.21(b) are spectra taken at room temperature with the PbWO_4 detector enabling all the fibres or only the T13 trigger channel respectively. Both are closer with the only difference of the number of events. With all the fibres enabled, there are much more events.

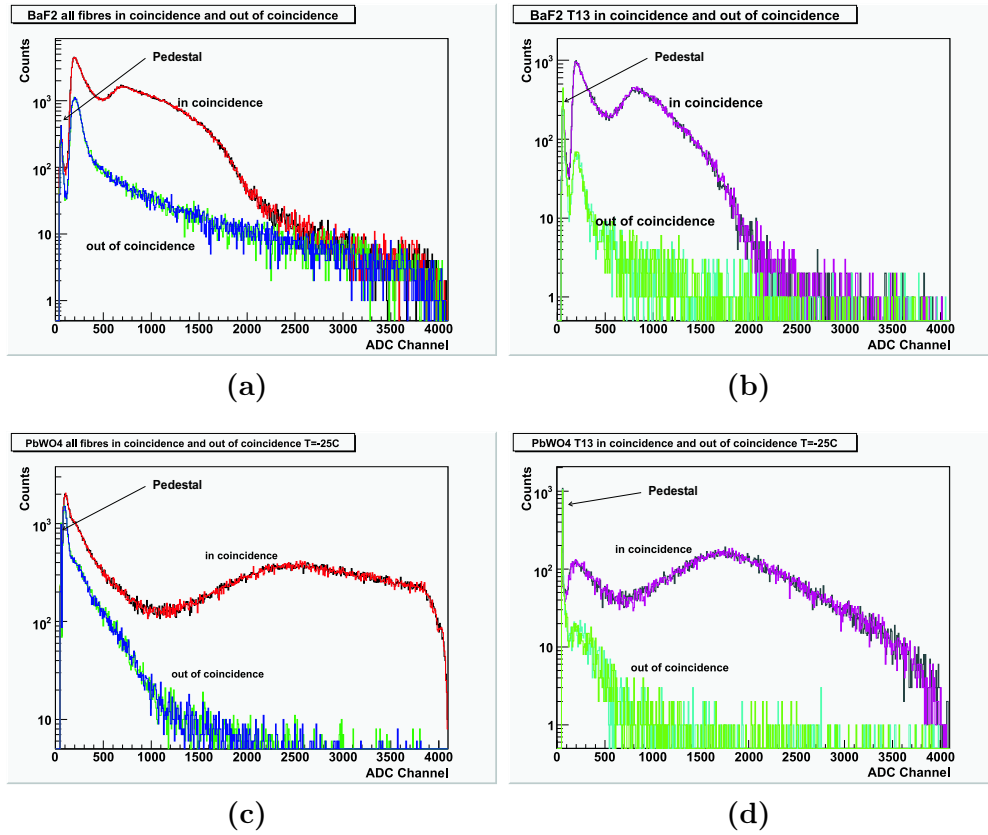


Figure 5.22: Comparison between BaF_2 and PbWO_4 : (a) All fibres in coincidence with BaF_2 ; (b) T13 in coincidence with BaF_2 ; (c) all fibres in coincidence at -25°C with PbWO_4 ; (d) T13 in coincidence at -25°C with PbWO_4 .

The figures 5.21(c) and 5.21(d) are the spectra taken at -25°C , with all the fibres and T13 in trigger respectively. In this case we have an amplification of approximately 3.5 times bigger than at room temperature, due to the enlargement of the light yield at low temperatures. Nevertheless, the difference between enabling all the fibres or only one fibre channel (as an example in this case T13) is not determinant.

From these measurements we can conclude almost the same as with the measurements with radioactive sources. Effectively, the light yield is greater at lower temperatures as is expected but the detector has too bad energy resolution. Therefore it is not useful for our purposes.

Then also measurements with the BaF_2 detector were taken, also in coincidence and out of coincidence. The spectra are plotted in figure 5.22.

Since these spectra are taken under the same conditions as with the PbWO_4 detector, without taking in account the temperature, we can com-

pare them. Spectra taken with both detectors are quite similar except by the fact that the data taken with the PbWO_4 seem to be expanded, but not well resolved. In turn, spectra taken with BaF_2 show better resolution, but still a lot of background at low energies.

The origin of this background was found in the vacuum chamber which contained the fibre detector. The electrons which were deviated from the beam line hit the steel in the vacuum chamber generating electromagnetic showers and particles with low energies. Some of those particles hit the fibre detector and others were detected in the photon calorimeter. Particles from such events will hit both detectors with almost the same timing as particles from “real” events from the interaction region do. Therefore this background could not be suppressed by the coincidence constraint.

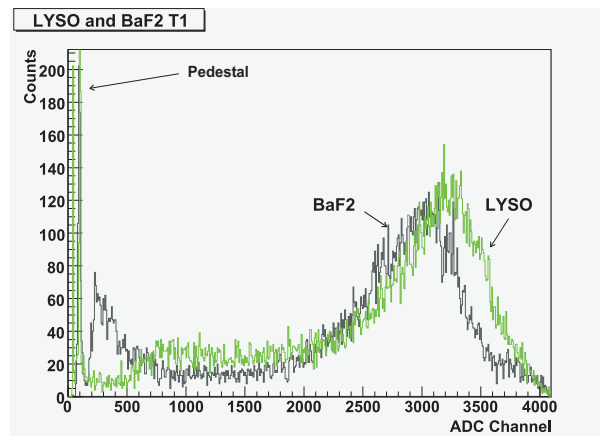
Shielding the detector from this secondary radiation, the most part of the background was removed.

In order to avoid the background in the LYSO detector, it was located inside a lead cylinder.

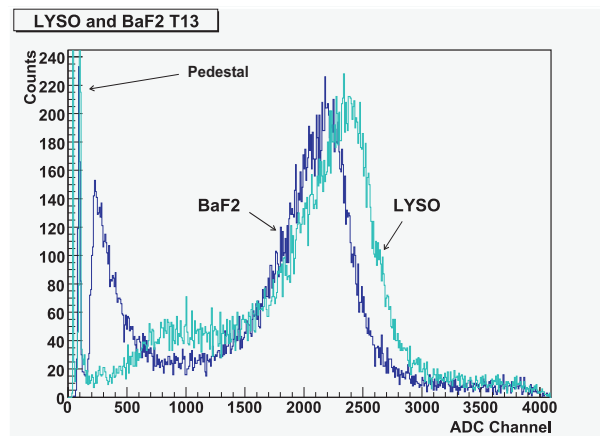
Comparison of the spectra taken with the BaF_2 and the LYSO detectors show that there are not so much differences between them (Figure 5.23). As one can see, the LYSO detector becomes less background than the BaF_2 due to the better shielding. It has to be taken in account that the spectra measured with the LYSO detector were taken with all the crystals but the high voltage not yet fully inter-calibrated. Only a first-fast inter-calibration was done looking at the amplitude of the pulses of the intrinsic radioactivity of the LYSO crystals on the oscilloscope screen changing the high voltage value. The chosen voltages were those which made that the amplitude of the radioactivity pulses the same for all crystals. Therefore the resolution is worse than expected. In principle, both detectors could be used to detect backscattered photons, but using the LYSO detector that has definitely better energy resolution will lead to smaller systematic errors in the analysis of the Compton asymmetries, as the Compton asymmetry is a function of the backscattered photon energy (see section 3.1). Measurements of backscattered photons were done with the LYSO detector but they will be shown later (see section 5.5).

5.4.2 Correlation Measurements

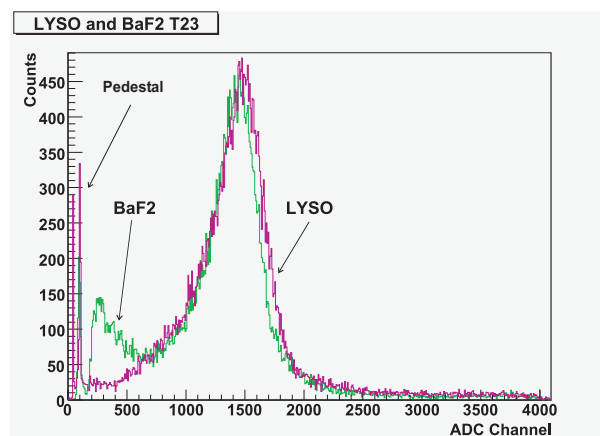
The idea of the correlation data taking is to trigger on coincidences between photon detector and any one of the fibres, to get spectra of tagged photons for all 24 fibres within one run (=5 min instead of 24 runs=several hours). All the fibres are enabled in the trigger electronics, so on the hard-



(a)



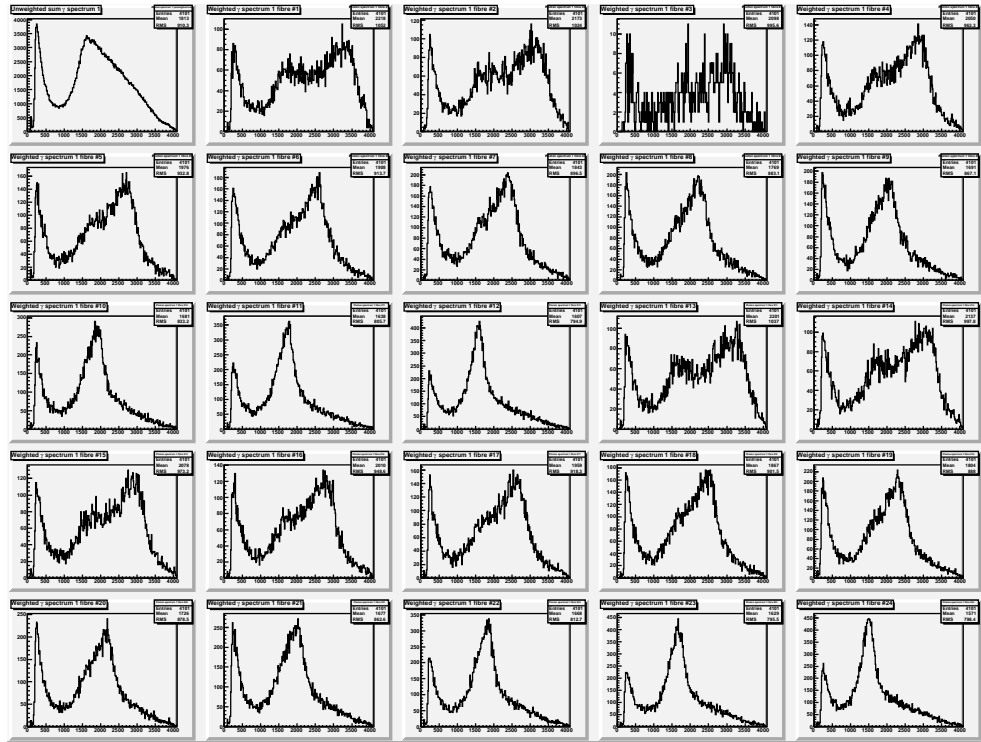
(b)



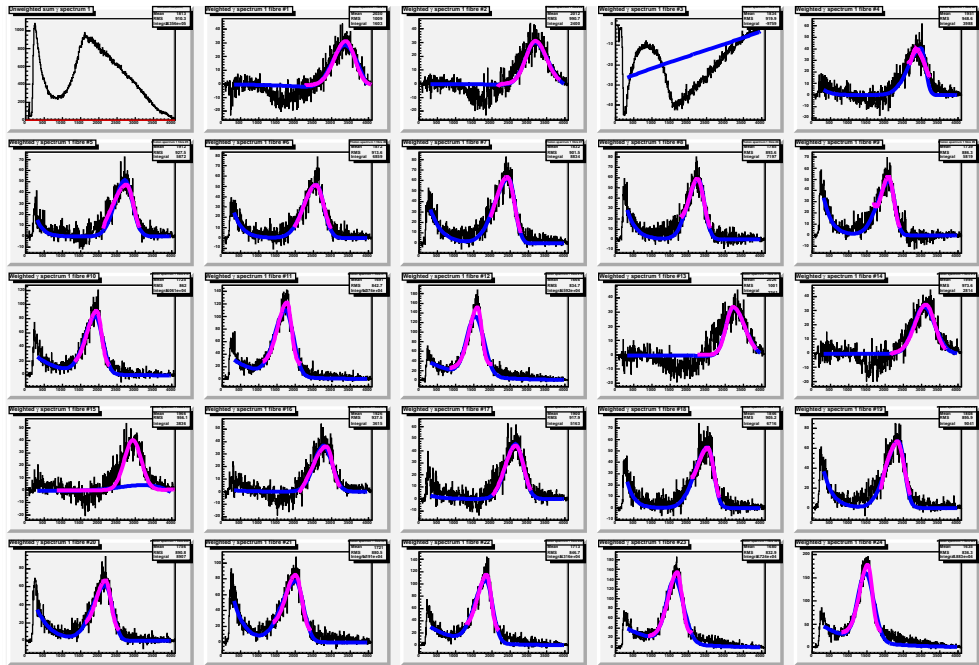
(c)

Figure 5.23: Comparison between BaF₂ and LYSO: (a) Only T1 in trigger; (b) only T13 in trigger; (c) only T23 in trigger.

5.4 Measurements with the beam



(a)



(b)

Figure 5.24: *Correlation measurements: (a) BaF₂ with a beam energy of 855 MeV; (b) Fit results for the correlation measurement. The first spectrum corresponds to the spectrum when all fibres are enabled. Note that the fibre number 3 does not work properly.*

ware side no information would be available on which fibre(s) were hit in an event. So far we just only know that a photon arrived in the LYSO and we had one (or more) hit(s) somewhere on the fibres.

This means we would not be able to tag our photons. Therefore we digitize the energy deposition for every fibre for our events - in addition to just only digitizing the energy deposition in the LYSO. For a single event, we get now 25 numbers: Edep(LYSO), Edep(fibre1), Edep(fibre2), ..., Edep(fibre24). The DAQ⁹ software compares the Edep value for every fibre with a given threshold value to decide which of the fibres have been hit in this event. According to this, we can now tell the amount of energy deposition in the LYSO and which of our fibres have seen a hit in coincidence with the LYSO.

The DAQ software creates 24 histograms to collect separate photon spectra for all 24 fibres.

The result of such a correlation run with all fibres enabled in the trigger electronics would be 24 photon spectra. Each of these spectra should look almost the same as if it was taken without correlation with all fibres disabled, except the fibre the spectrum belongs to.

In figure 5.24(a) one can see, as an example, a correlation spectrum taken for the BaF₂ at 855 MeV of beam energy. The first histogram is the spectrum of all events, that is the spectrum when all fibres are enabled. On the others, one can clearly see the peaks corresponding to each fibre, but over a background which has more or less the same shape as the total spectrum but scaled.

In the figure 5.24(b) one can see the results of the fit of the peak positions for each fibres. The fit function which has been used is an asymmetric gaussian plus an exponential. The values of the χ/ν were in almost all cases quite big. The fits must be improved. But from these measurements a first energy calibration using high energies can be done.

Energy calibration

By knowing the position of each fibre and the beam energy when the correlation measurement is done, one can calculate the energy which the photon peak is related to. We can perform an energy calibration in the energy ranges in which the electron detector is working.

One can know the position of the fibre detector doing a position scan which moves a guide wire and the fibre detector through the beam, which is turned for this purpose to very low current. This guide wire is parallel

⁹Data Acquisition Software.

to the fibres and it is fixed at a known distance. When this wire crosses the beam, secondary radiation is produced. This radiation is detected with a leadglass detector and recorded together with the fibre detector position. When the detector starts to move into the beam, also this secondary radiation is detected in the leadglass detector and one can see an edge in the spectra. Measuring the distance between the peak generated by the radiation in the wire and the edge we can calculate how far from the beam the fibre detector is at its home position. This method is not perfect, because is difficult to say where exactly the electron detector starts due to the shape of the edge. It is planned to put another wire between the first one and the fibre detector in order to have two peaks at a measurable distance in the spectra and not only one peak and an edge.

Then as we know the dimensions of the fibres and the deviation of the electrons from their original trajectory related with their energy loss, we can calculate the energy each fibre is related to.

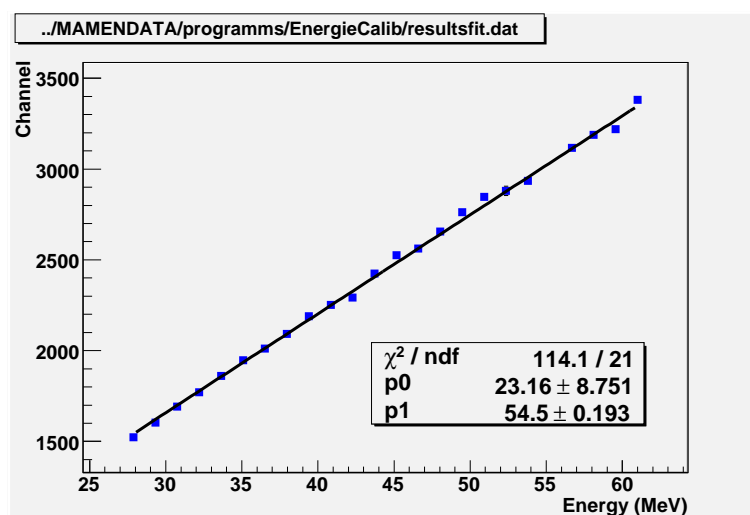


Figure 5.25: *Energy calibration from correlation measurement.*

Preliminary results for this energy calibration are represented in figure 5.25 for the BaF₂ detector. The value of the χ^2/ν is not good. Using for the fit a second degree polynomial function, its value is almost the same. The values of the χ^2/ν in the determination of the peak positions from the correlation data are also too big in almost all cases, and an improvement in its determination is needed. The results in the cases of LYSO detector are close to these. Several sources of systematical errors have to be determined and controlled, as for example the variation in the magnetic field in the dipoles, the position of the fibre detector or with which accuracy the relative position of the fibres is known. These errors can not be calculated for these last measurements and they have to be determined in the next beam time in order to

improve the results. For a beam energy of 315 MeV one can also include the peaks from the AmBe source in order to introduce data points of well known energy. It will be done during one of the next beam times.

5.4.3 LYSO high voltage calibration

Due to the detector geometry, nine photomultipliers have been used. Obviously, their response is different, so that we have to find a way to calibrate them to get the same response to the same energy deposition for each crystal. Also the attachment of the photomultipliers to the crystals and the quantum efficiency of them can influence this response.

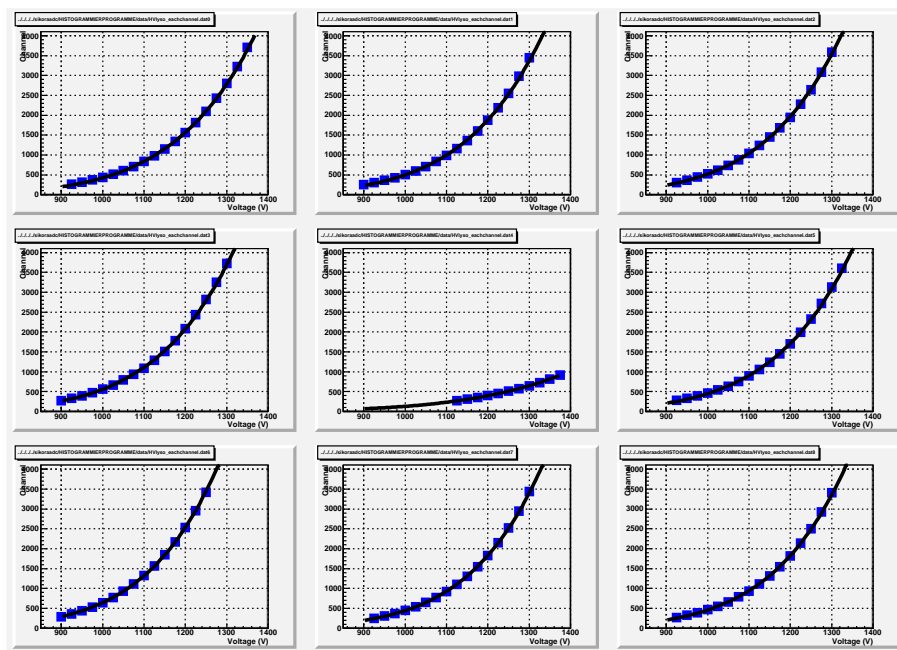


Figure 5.26: *Results of the first HV calibration.*

In order to perform a high voltage calibration, spectra with a ^{60}Co source were taken, using in each case only one of the crystals of the detector and changing the values of the voltages. Measurements of 5 minutes were done and the voltages were changed from 900 V up to 1375 V. The measurements were taken automatically using a script.

The next step was to measure the position of the second ^{60}Co line for each voltage and each crystal to fit a calibration curve ADC Channel vs. high voltage. The figure 5.26 shows the results of these calibrations. As one can see, the central detector had less gain than the others.

This method was useful only to have an approximate high voltage for

each photomultiplier, but the detector was not yet fully calibrated. Factors such as drift in the photomultipliers or instability of the power supply can influence this first calibration. A program to calculate how much the high voltage has to be changed to move the second peak of the ^{60}Co source to the desired position, was developed.

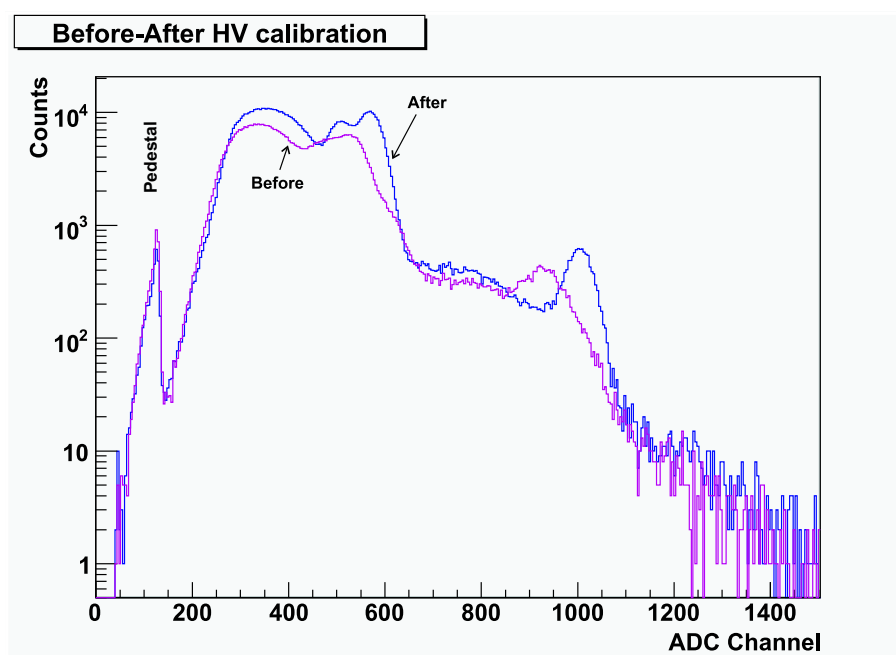


Figure 5.27: Two spectra before and after the HV calibration.

This program uses the actual values of the high voltage and measures the position of the second peak of ^{60}Co in each channel.

The peak position changes with the voltage as follows:

$$Ch = a \cdot V^b \quad (5.9)$$

where Ch represents the ADC Channel and V is the applied voltage.

If the changes in the voltages are small, we can approximate its behavior as a straight line around our position. Then we consider the derivative:

$$\frac{dCh}{dV} = ab \cdot V^{b-1} \quad (5.10)$$

which can be written as follows for finite intervals:

$$\Delta V = \frac{\Delta Ch}{ab} \cdot V^{1-b} \quad (5.11)$$

Then we can improve the calibration, knowing the old values for the high voltage and the peak positions for each crystal.

In the figure 5.27 we can see the effects of this improvement. In the spectrum taken before the high voltage calibration the sum of the signals coming from the different crystals does not permit to have a good energy resolution. In the sum of the signal after the high voltage calibration, the spectrum shows the two peaks of ^{60}Co clearly resolved.

After the first high voltage calibration, the photomultiplier of the crystal with less gain was changed in order to know whether the problem comes from it or from the crystal. The voltage calibration was repeated and the calibration curve showed better results for this detector.

The last step done was to change the passive voltage dividers by active voltage dividers. The results of the high voltage calibration were again satisfactory.

5.5 Measurement of backscattered photons

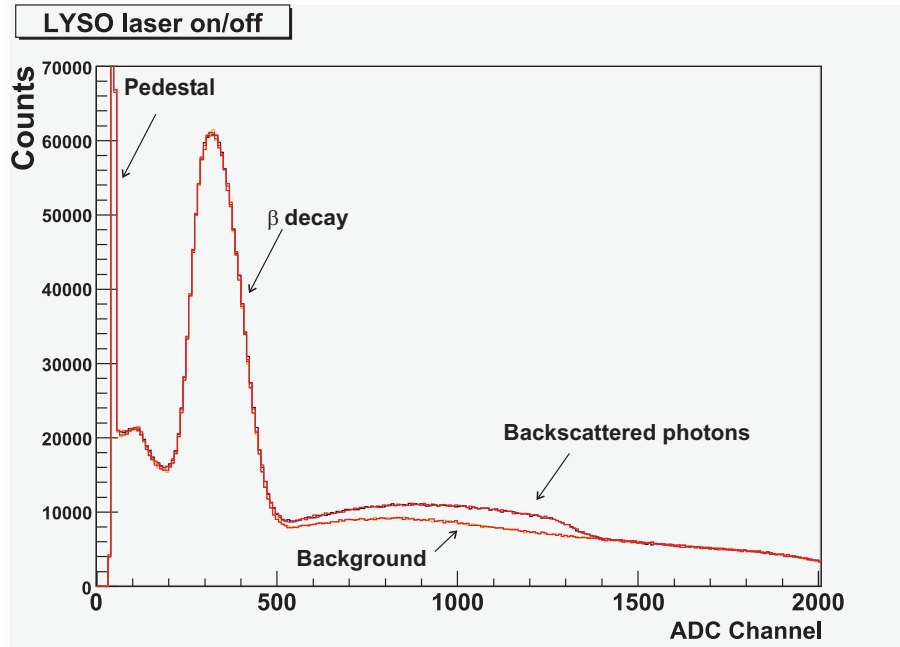


Figure 5.28: *Backscattered photons and background spectra detected in LYSO.*

The first measurements of backscattered photons since two years ago were done with the LYSO detector. It is expected to be better than the BaF_2 , and definitively much better than the PbWO_4 . Measurements with other

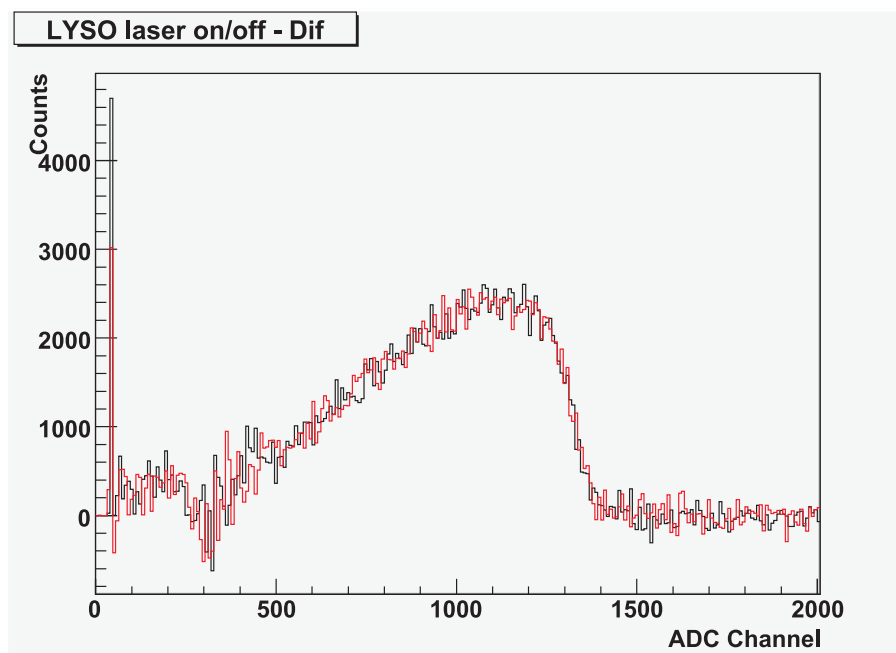


Figure 5.29: *Difference between backscattered photons and background detected in the photon calorimeter.*

detectors have not yet been done. In figure 5.28 one can see the spectra of the backscattered photons and bremsstrahlung background. Note that each of them contains two colors, each one corresponding to positive or negative beam helicity.

If the difference between both is calculated we obtain the spectrum of the backscattered photons (figure 5.29).

Then measuring the counts for each polarization, one can obtain the first preliminary values for the asymmetry and consequently a first measurement of the beam polarization.

It is important to say that these measurements were taken when the LYSO detector was not yet fully high voltage inter-calibrated. So that they can be taken in account as an example of the measurement process.

During the next beam time it is expected to measure with the detector fully calibrated and it will be possible to obtain the first measurements of the beam polarization online with the whole experiment running.

Chapter 6

Conclusions and outlook

In the scope of this work three different materials have been tested for the photon calorimeter of the A4-Compton backscattering polarimeter.

Detectors of PbWO_4 , BaF_2 , and LYSO have been developed and put into operation. Properties as the energy resolution, or linearity have been determined and compared. The manageability of the detectors has also been taken in account.

For this purpose, measurements with radioactive sources and measurements with the beam of the MAMI have been done and the software for the data analysis and the energy calibration of the detectors has been developed.

The data acquisition electronics have been also improved and documented. A problem with the ADC, which had caused severe troubles when trying to understand the spectra, has been found and solved.

It has been found that the PbWO_4 detector was not suitable for our purposes and it has been put out. The BaF_2 could be used, but the tests performed with the LYSO detector showed that it has definitively better energy resolution and high stability. Its dimensions were also small and the mechanical construction, as well as being stable, permits to change the photomultipliers easily if needed.

Therefore, this detector has been put behind the interaction region of the A4-Compton polarimeter into a lead cylinder to shield it from the background which comes from the beam line. It is being used to measure the polarization.

To use nine crystals instead of only one, makes a high voltage inter-calibration for the photomultipliers necessary. Therefore a method to do that has been developed and it has been successfully used with different types of photomultipliers which have been used, as well as for the passive or active voltage dividers. The high voltage can be calibrated in breaks of maximal 30 minutes without beam. During the last beam time the inter-calibration routine was used as a routine tool.

Chapter 6. Conclusions and outlook

The active voltage dividers have been tested and they worked properly. Rates up to 80 – 100 kHz can be now measured with the beam on. No differences in the spectra have been found.

The correlation measurements with the fibre detector do work now. They are to be used in the future for understanding the detector properties and provide an energy calibration at photon energies above the range available with radioactive sources. The unexpected background found in the correlation data has not yet been understood, but a first approach to deal with it, which should be further improved, has been found.

Preliminary data were taken with the LYSO detector, in a polarimeter test beam time in March 2007. Then, for the very first time Compton data have been taken in the August beam time 2007 with the main experiment running. The polarization of the beam will be extracted from these data in the following weeks.

List of Figures

2.1	<i>Feynman diagram for the scattering of electrons off protons.</i>	4
2.2	<i>Experimental setup of the A4 experiment.</i>	6
3.1	<i>Kinematics of Compton effect.</i>	10
3.2	<i>Compton scattering and the polarization of the electrons.</i>	11
3.3	<i>Unpolarized cross section of the Compton effect.</i>	13
3.4	<i>Polarized cross section of the Compton effect.</i>	14
3.5	<i>Compton asymmetry.</i>	14
3.6	<i>Schematic drawing of the Compton backscattering polarimeter.</i>	15
3.7	<i>Schematic drawing of Laser and resonator.</i>	17
3.8	<i>Schematic drawing of the wire scanners.</i>	18
3.9	<i>AutoCad drawing of A4-Compton Backscattering Polarimeter.</i>	19
3.10	<i>Actual fibre detector.</i>	20
3.11	<i>Schematic drawing of the fibres layout.</i>	21
3.12	<i>Simple schema of the electronics.</i>	22
3.13	<i>3D view of A4-Compton backscattering polarimeter.</i>	24
4.1	<i>PbWO₄ and BaF₂ detectors.</i>	29
4.2	<i>Schematic drawing of the cooling system.</i>	30
4.3	<i>LYSO crystal.</i>	31
4.4	<i>Reflective foil.</i>	32
4.5	<i>LYSO wrapped in reflective foil.</i>	33
4.6	<i>LYSO intrinsic radioactivity decay scheme.</i>	33

List of figures

4.7	LYSO detector.	34
5.1	Examples of the dark current and LED pulses.	36
5.2	Gain measurement.	38
5.3	Transmission spectra for LYSO and PbWO_4	39
5.4	^{60}Co spectra measured with PbWO_4 at room temperature.	41
5.5	Muon spectra measured with PbWO_4 at room temperature.	41
5.6	^{60}Co lines and muons simulation.	42
5.7	Spectra simulation for the PbWO_4	44
5.8	^{60}Co measured with PbWO_4 with PbWO_4 spectra at -25°C	45
5.9	Muon spectra measured with PbWO_4 at -25°C	45
5.10	AmBe spectra measured with PbWO_4 at room temperature.	47
5.11	AmBespectra measured with PbWO_4 at -25°C	47
5.12	Spectra with BaF_2	48
5.13	BaF_2 energy calibration.	49
5.14	Spectra taken with LYSO central crystal.	51
5.15	Radioactive spectra taken with full LYSO detector.	53
5.16	LYSO energy calibration.	54
5.17	LYSO energy calibration central crystal.	54
5.18	Pulser spectrum.	56
5.19	Test with pulser fit result.	56
5.20	Delay curve.	57
5.21	PbWO_4 spectra at different temperatures.	59
5.22	comparison between BaF_2 and PbWO_4	60
5.23	Comparison between BaF_2 and LYSO.	62
5.24	Correlation measurements.	63
5.25	Energy calibration from correlation measurement.	65
5.26	First energy calibration.	66
5.27	Spectra before (Pink) and after (Blue) the HV calibration.	67
5.28	Backscattered photons in LYSO.	68

5.29 *Difference between backscattered photons and background detected in the photon calorimeter.* 69

List of Tables

4.1	<i>Principal characteristics of the different scintillator materials [Par].</i>	28
4.2	<i>Energy ranges of detected photons as a function of the beam energy.</i>	32
5.1	<i>Test of the photomultipliers with the LED.</i>	37
5.2	<i>Measurement of the gain of the photomultipliers.</i>	37
5.3	<i>Energy resolution for BaF₂.</i>	50
5.4	<i>Energy resolution of BaF₂ calculated by TAPS collaboration [Sch89].</i>	50
5.5	<i>Energy resolution for LYSO.</i>	52
5.6	<i>Attenuation.</i>	55

Bibliography

- [B⁺07] L. Bardelli et al. Pulse-shape discrimination with PbWO₄ crystal scintillators. *Nucl.Instrum.Meth.*, June 2007.
- [BR03] Phillip R. Bevington and D. Keith Robinson. *Data Reduction and Error Analysis for the physical sciences*. McGraw-Hill Higher Education, 2003.
- [Glä05] Boris Fabian Gläser. Entwicklung und Realisierung eines experimentellen Aufbaus für die Messung der paritätsverletzenden Asymmetrie in Elektron-Proton-Streuung unter Rückwärtswinkeln, Januar 2005.
- [Ima03] Yoshio Imai. Entwicklung eines optischen Systems für ein Compton-Rückstreupolarimeter, Februar 2003.
- [Lee] Jeong Han Lee. In development. PhD thesis, Institut für Kernphysik, Johannes Gutenberg-Universität Mainz.
- [LG96] Amilcar Lopes Ginja. Vorstudien zum Bau eines Polarisationsmonitors für ein paritätverletzendes Experiment, Dezember 1996.
- [M⁺94] M. J. Musolf et al. Intermediate-energy semileptonic probes of the hadronic neutral current. *Phys. Rept.*, 239:1–178, 1994.
- [M⁺04] F. E. Maas et al. Measurement of Strange-Quark Contributions to the Nucleon's Form Factors at $Q^2 = 0.230 \text{ (GeV/c)}^2$. *Physical Review Letters*, 93(2):022002, 2004.
- [M⁺05] F. E. Maas et al. Evidence for Strange-Quark Contributions to the Nucleon's Form Factors at $Q^2 = 0.108 \text{ (GeV/c)}^2$. *Physical Review Letters*, 94(15):152001, 2005.
- [MF02] Carole Marmonier and S-O Flyckt. *Photomultiplier tubes - Principles and applications*. Photonis, September 2002.
- [Par] Particle Data Group. Particle physics booklet.

Bibliography

- [Sch89] Matthias Schneider. Test von BaF₂-Detektoren zum Aufbau eines π^0 -Spectrometers, Juni 1989.
- [Sik04] Mario Sikora. Aufbau und Inbetriebnahme eines Natriumiodid-Detektors für das A4-Comptonpolarimeter, Juni 2004.
- [Str00] Oliver Strähle. Aufbau und Inbetriebnahme des A1-Möllerpolarimeters, April 2000.
- [Thi05] Michaela Thiel. Calorimeter readout with large area avalanche photodiodes, 2005. Workshop on physics with antiprotons.
- [Wei00] Christoph Weinrich. Entwicklung eines Transmissions-Compton-Polarimeters für das A4-Experiment, Juli 2000.

Danksagung

Acknowledgments

Agradecimientos

Agraïments

Jetzt da ich mit meiner Diplomarbeit fertig bin, möchte ich gerne allen danken, die mir geholfen haben.

Mein Dank geht an Prof. Dr. Dietrich von Harrach, der mir einen Platz in der A4-Kollaboration gegeben hat. Ich möchte mich auch bei Dr. Frank Maas bedanken. Er war ein guter Betreuer während meiner Zeit als SEACAVA-Sommer-Studentin und hat zu meiner Entscheidung, in Mainz die Diplomarbeit zu machen, beigetragen.

Jürgen hat mir sehr mit meiner Diplomarbeit geholfen, aber auch viel zu meinen Deutschkenntnissen beigetragen.

Mein Dank geht auch an die Mitarbeiter von A4: Yoshio und Jeong Han waren bei Computerproblemen immer da. Sebastian, Luigi, Boris, Christoph und Reiner haben für ein tolles Arbeitsklima gesorgt und waren auch nach der Arbeit immer sehr gesellig.

Ei, Mathilde, I can not forget you. You have been also a good friend.

Nun zu den Spaniern....

Pues sí, ahora cambiamos de idioma. En primer lugar quiero agradecer, por supuesto, a SEACAVA, por ofrecerme la oportunidad de participar en el "SUMMER PROGRAM '04" (Si los cálculos no me fallan...). Aquel verano fue BRUTAL y gracias a ello estoy ahora escribiendo esto. Luego, la verdad, es difícil decidir por quién empezar. Seguro que se me olvida alguien. Además ha habido varias etapas desde que estoy aquí.

Recuerdo cuando tomábamos birra en el bar de "la Jejaim" todos los Lunes y Miércoles. Después, cuando me auto-invataba a comer a casa de Micha. Pobre hombre, todo lo que ha tenido que aguantarme. Y más tarde cuando me pasaba casi todos los "findes" en casa de Marta y Andi. También

Danksagung, Acknowledgements, Agradecimientos, Agraïments

me pasé algunos cuándo os fuisteis a vivir con Ana y Fer.

Quedar con Fidel es un poco más difícil, puesto que vive a 15 minutos de todas partes, pero en fin...

Cristina y Mauri, a pesar de vivir un poco lejos de la Civilización, siempre estáis ahí. Mauri para hacer una excursión “que te cagas” por el río y Cris para ponerse “golfa” de vez en cuando. Además me acogisteis unos días en vuestra casa hasta que tuve la residencia cuando llegué de vuelta.

Raquel ens ha ensenyat que “un quart de tres” vol dir “les dos i quart”. Tranquila, ara que tindrè un poquet més de temps, jugarem alguna altra “Futpatxanga”.

Salva, me encanta el entusiasmo que sigues teniendo por cualquier parte de la física y no sabes la envidia que me das con tus inventos. He aprendido mucho y me lo he pasado muy bien contigo.

David y Aitsa, gracias por las invitaciones a cenar a vuestra casa y también gracias por aceptar las mías.

Nando, Enrique, Patricia, no me puedo olvidar tampoco de las meriendas en la mensa, por nombrar alguna de las experiencias vividas juntos.

Por supuesto los Erasmus españoles, tanto los de mi año como los que han estado aquí este año. Aunque no os nombre me acuerdo de vosotros.

Of course, I can not forget all the people from other countries that I met here. The possibility of speak in 4 or more languages during the lunch is amazing.

Hay mucha más gente de la que también me estoy acordando y que ya no está aquí o con la que he perdido un poco el contacto, pero no por ello dejo de acordarme de vosotros y de todos los momentos vividos juntos. También os quiero dar las gracias, por haber formado parte de mi vida en algún momento. Sí, aunque tu nombre no aparezca, también he pensado en ti.

Por fin hay alguien de quien por supuesto que me acuerdo, pero me dijo que no quería salir en los agradecimientos. ¿Conseguirás tu objetivo con esto?

Y ahora tengo que viajar a España. Aquí también hay mucha gente a la que tengo que agradecerle un montón de cosas.

A mis amigos de Quart, se que me echáis de menos y también se que vais a estar ahí siempre. Vosotros ya sabéis quiénes sois, no hace falta que os nombre a todos.

Ahora llega el momento de dar las gracias por la educación recibida. Por supuesto a todos los profesores que a lo largo de mi vida me han aportado algo. Sobre todo quiero darle las gracias a José María, porque “por su culpa”

acabé estudiando Física.

I ara per fi em toca parlar en la meua llengua. Gràcies a tota la familia per estar ahí. Als meus tíos i els meus cosins, moltes gràcies. A la iaia, que no compren què es això de la física, però que si a mí m'agrada, avant. L'agüela encara no se n'ha adonat de que no estudie Astrofísica, però si ella està contenta diguent-li-ho a la gent, m'alegre. I la tia Nieves mai diu res, aixina que jo tampoc dic res.

Sobre tot moltes gràcies a l'agüelo i al tío Nofre. Gràcies a d'ells sempre he tingut interès per la ciència i el coneixement. Tal volta també ha ajudat el que m'anomenaren "*carabasseta sabia*".

Gràcies a Jo i a I. Sempre estem renyint, pero es normal. Som germans.

I per fi, moltes gràcies a mons pares. Que son els que m'han donat una educació desde ben menudeta.

Ich erkläre hiermit, dass ich die vorliegende Arbeit selbständig verfasst habe und keine anderen als die angegebenen Quellen und Hilfsmittel verwandt habe.

Mainz, den 14. August 2007

María Carmen Mora Espí

